

Laser-Assisted Structuring of Graphene Films with Biocompatible Liquid Crystal Polymer for Skin/Brain-Interfaced Electrodes

Rowoon Park, Dong Hyeon Lee, Chin Su Koh, Young Woo Kwon, Seon Yeong Chae, Chang-Seok Kim, Hyun Ho Jung,* Joonsoo Jeong,* and Suck Won Hong*

The work presented here introduces a facile strategy for the development of flexible and stretchable electrodes that harness the robust characteristics of carbon nanomaterials through laser processing techniques on a liquid crystal polymer (LCP) film. By utilizing LCP film as a biocompatible electronic substrate, control is demonstrated over the laser irradiation parameters to achieve efficient pattern generation and transfer printing processes, thereby yielding highly conductive laser-induced graphene (LIG) bioelectrodes. To enhance the resolution of the patterned LIG film, shadow masks are employed during laser scanning on the LCP film surface. This approach is compatible with surface-mounted device integration, enabling the circuit writing of LIG/LCP materials in a flexible format. Moreover, kirigami-inspired on-skin bioelectrodes are introduced that exhibit reasonable stretchability, enabling independent connections to healthcare hardware platforms for electrocardiogram (ECG) and electromyography (EMG) measurements. Additionally, a brain-interfaced LIG microelectrode array is proposed that combines mechanically compliant architectures with LCP encapsulation for stimulation and recording purposes, leveraging their advantageous structural features and superior electrochemical properties. This developed approach offers a cost-effective and scalable route for producing patterned arrays of laser-converted graphene as bioelectrodes. These bioelectrodes serve as ideal circuit-enabled flexible substrates with long-term reliability in the ionic environment of the human body.

1. Introduction

Due to extreme simplicity in production and their exceptional electrical properties, laser-induced graphene (LIG) materials have attracted great attention for a wide range of applications, including electronics, energy storage, chemical sensors, and bioengineering.^[1-3] Along with advances in micro-laser fabrication methods, LIG materials have made significant progress in achieving high electrical conductivity, mechanical strength, and thermal stability, making them a major research area of interest in carbon nanomaterials as attractive candidates for the circuit components for next-generation devices.^[4] The practical development of LIG materials has been focused on improving their physical and chemical properties by exploring suitable manufacturing processes that yield outstanding material characteristics, on par with other conductive films. One of the most significant recent breakthroughs in LIG production techniques is the ability to fabricate LIG films on a large scale using solution-casted polyimide (PI) thin film or photoresist at a production speed of approximately

R. Park, C.-S. Kim, S. W. Hong
Department of Optics and Mechatronics Engineering, Department of
Cogno-Mechatronics Engineering, College of Nanoscience and
Nanotechnology
Pusan National University
Busan 46241, Republic of Korea
E-mail: swhong@pusan.ac.kr

D. H. Lee
School of Mechanical Engineering
Pusan National University
Busan 46241, Republic of Korea
C. S. Koh, H. H. Jung
Department of Neurosurgery
College of Medicine
Yonsei University
Seoul 03722, Republic of Korea
E-mail: junghh@yuhs.ac

Y. W. Kwon, S. Y. Chae, C.-S. Kim, S. W. Hong
Engineering Research Center for Color-Modulated Extra-Sensory Perception
Technology
Pusan National University
Busan 46241, Republic of Korea

 The ORCID identification number(s) for the author(s) of this article can be found under <https://doi.org/10.1002/adhm.202301753>

© 2023 The Authors. Advanced Healthcare Materials published by Wiley-VCH GmbH. This is an open access article under the terms of the [Creative Commons Attribution-NonCommercial](#) License, which permits use, distribution and reproduction in any medium, provided the original work is properly cited and is not used for commercial purposes.

DOI: 10.1002/adhm.202301753

150–200 mm s⁻¹ while maintaining high resolution ranging from micro to millimeters.^[5–7] Compared to other synthetic routes to produce graphene, such as chemical vapor deposition (CVD) and acidic exfoliation process, this progress holds the potential for high-throughput production of qualified graphene-based films in an economically viable and environmentally friendly manner.

In most cases, the fabrication process of LIG material involves the use of a programmable optical setup (i.e., laser irradiating system) and the precursor film (e.g., PI) with appropriated carbon content.^[8] Thus, a film type of patterned LIG can be easily fabricated by fully established mechanisms of photochemical and/or photothermal conversion,^[9] which includes the localized chemical transformation of precursor molecules at the thermally activated state. In terms of film or bulky precursors, the focused irradiating laser could be applied to a wide range of materials, such as polymers, paper, textiles, leaf, and even wood waste.^[10–12] This implies that the low cost of the starting materials suggests an attractive option for the scalable production of high-performance carbon nanomaterials. Further, by carefully selecting the wavelength of the laser source, the significant aspect of LIG in the practical development can be extended to another field of study, such as ultrathin graphene optics, with the help of the advanced optical component.^[13] Thus, the versatility of LIG fabrication methods using different materials underscores their potential to meet specific requirements across a wide range of applications, including but not limited to flexible electronics, sensors, energy storage devices, and even biomedical applications.^[14]

In this context, among other material systems for the thin film approach, some proper types of LIG-based graphene materials have been explored as advantageous substrates of the intriguing architectures in the biological interface, due to their unique physicochemical properties, nontoxic biocompatibility, appropriate mechanical strength, and versatile interactions with specific biomolecules.^[15,16] In addition, LIG has great advantages in bio-integrated electrodes, such as biosensors, diagnostic devices, implantable electrocorticography (ECoG), or neural stimulation. For example, LIG-based biosensors have been developed for various biomolecule detection, which offer several advantages over traditional electrodes with the high surface area and ability to be functionalized with different biomolecules, such as proteins and antibodies, which allow for the efficient immobilization of target molecules to improve sensitivity/specificity, reproducibility, and stability of the biosensors.^[17] Similarly, in the field of brain interface, LIG has also represented great potential as a patterned electrode array that does not cause harm or side effects when in contact with living tissues due to its superior biocompatibility.^[18,19] Owing to the additional high conductivity of LIG-based electrodes, the brain-interfaced electronic integration could be one possible access to record electrical signals from the neuronal

activities that have several biomedical applications, such as diagnosing epilepsy and studying brain function.^[20,21] However, the above-suggested works mainly rely on the quality of the LIG films with high resolution and related mechanical and electrical reliability. More importantly, as the basis for passive electrodes, the patterned LIG-embedded substrate with sufficient biocompatibility provides design opportunities with respect to an efficient transfer onto the tissue substrate without the degradation of key requirements. Some exploratory solutions for LIG may make them possible for use in healthcare monitoring electronics with diagnostic or therapeutic functions during a biological process.^[22]

Here, we introduce a new source material for fabricating LIG films, along with the relevant processing techniques, to produce flexible or stretchable bioelectrodes that are designed for applications on diverse biological tissue surfaces, such as human skin and animal brains. Inspired by the aforementioned advantages, especially those of alternative biocompatible electronic substrates, we first demonstrate the use of liquid crystal polymer (LCP) film as the primary LIG material. The manufacturing process involves precise control of laser scribing parameters, pattern transfer, and subsequent printing steps to fully utilize the inherent structural characteristics of the LCP source material. Moreover, our approach exploited the high-throughput strategy for densely patterned LIG films, creating value-added bioelectrode arrays in a laminated configuration. We employed transfer printing to apply the patterned LIG films onto various receiving substrates, effectively transforming them into LIG-based printed circuit boards, which can also be encapsulated using a soft elastomer for added protection and mechanical robustness. This approach was demonstrated through the implementation of LIG-based circuit interconnects, integrating surface-mount devices (SMDs) while ensuring reliable electrical connections. To evaluate the utility of bioelectrodes, our first demonstrations focused on the highly sensitive on-skin bioelectrodes designed for use in electrocardiogram (ECG) and electromyography (EMG) applications with a flexible or stretchable design, offering several advantages as they serve as independently functional units connected to healthcare hardware platforms. In the following, utilizing a straightforward electrochemical approach, additionally presented LIG biosensors also exhibited excellent sensitivity and stability in detecting skin-related cytokine (i.e., TNF- α) detection. Finally, the key features of LIG microelectrode arrays interfacing with brain tissue involve their integration with mechanically compliant architectures, comprised of functional current source/encapsulant materials for neural stimulation and recording neuronal signals. Accordingly, in view of primary substrate material, the single ply of LCP film intrinsically indicates a superior property on low moisture absorption (i.e., <0.04%) than PI film (i.e., \approx 2.8%) commonly used for LIG processing, which makes it a perfect fit as an ideal substrate and encapsulant for the body's ionic environment with long-term reliability compared to other polymeric films.^[23] We believe that the LCP-based LIG method may provide a simple but viable route to produce laser-converted graphene films for biocompatible bioelectrodes with low cost, scalability, and the ability to directly transferable encapsulant onto a variety of substrates.

J. Jeong
School of Biomedical Convergence Engineering
Department of Information Convergence Engineering
Pusan National University
Yangsan 50612, Republic of Korea
E-mail: joonsoo_jeong@pusan.ac.kr

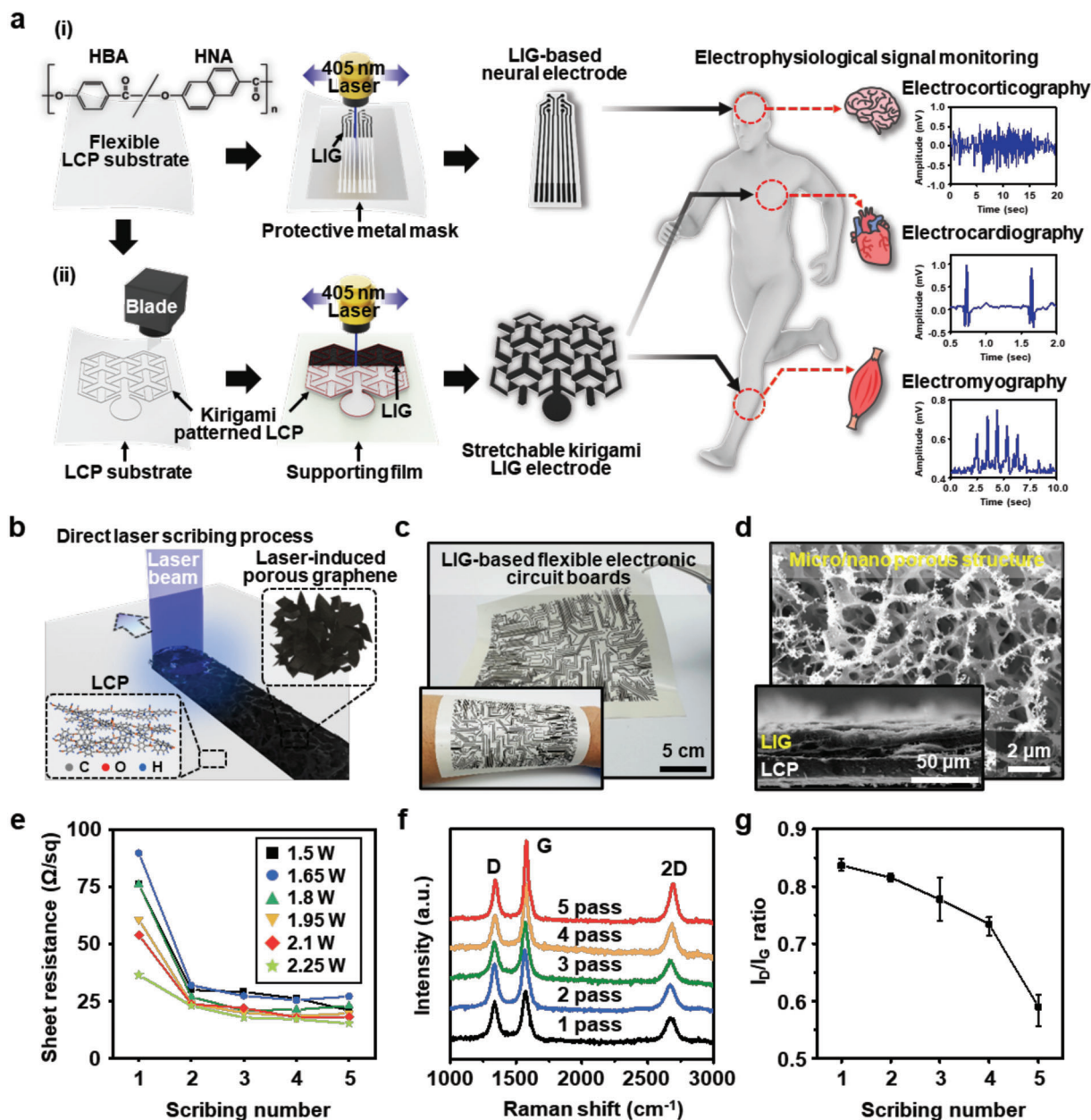


Figure 1. a) Scheme to produce LIG-based bioelectrodes for skin/brain interface, collecting electrophysiological signals such as brain activity (ECoG), cardiac activity (ECG), and muscle activity (EMG). b) Schematic diagram of the formation of LIG structure on the LCP substrate by using a laser beam irradiation system. c) The digital image of the LIG-based circuit array fabricated through a direct laser writing process (inset: an example of a scalable wearable circuit board). d) SEM image of the surface LIG consisted of micro/nanoporous structure (inset: a cross-sectional view of LIG film formed on LCP substrate). e) Improved conductivity by tuning of laser power and the number of scans. f,g) Raman spectra from the LIG film and statistical results of intensity ratios of D and G peak, as a function of the number of laser scans at an optimized laser power (2.25 W).

2. Results and Discussion

2.1. Multifunctional LIG-Based Bioelectrodes for Recording Electrophysiological Signals

Figure 1a–c describes the scheme of the manufacturing process for the patterned LIG film and the applications of the biointerfaces electrodes, using focused laser irradiation (450 nm) on an LCP film (i.e., $t = 25 \mu\text{m}$, Vecstar CTQ-25, Kuraray) by

photo-thermal transformation. As presented in Figure 1a, the LCP film used in this experiment is a block copolymer (inset chemical structure) composed of rigid (i.e., aromatic rings) and flexible segments (i.e., acyl groups) on a monomeric basis of 2,6-hydroxynaphthoic acid (HNA) and 4-hydroxybenzoic acid (HBA).^[24–26] Based on this chemical structure, we hypothesized that the surface of the LCP film rich in aromatic compounds could be fully carbonized by focused laser irradiation. In addition, we expected that the quality of the LIG film could be secured

with good mechanical properties and high-temperature durability due to the high crystallinity of the LCP film originating from the orderly arrangement of the rigid aromatic backbone.^[27,28] It is worth noting that our experimental concept is for the first time to produce LIG electrodes using an LCP film. Recently, the LCP film has garnered attention as an alternative biocompatible polymer to ensure reliability for implantable biomedical devices, especially for superior biofluid barrier properties with lower water molecules and gas permeability.^[29] This intrinsic material property is highly recommended by sufficiently tolerating a harsh ionic environment when surrounded by body fluids.^[30] With this unique material system, we performed the laser-scribing with two different approaches on the LCP film (Figure 1a), which include i) protective microscale shadow masking and ii) programmed scanner-based direct writing. Another option was also adapted for the mechanically predefined-cut LCP substrate and subsequently performed laser irradiation to transform the whole substrate into graphene-structured film. This approach is highly useful for designing patch-type stretchable bioelectrodes by adopting a kirigami configuration with structural advantages. Figure 1a schematically represents the scheme of the ECoG, ECG, and EMG applications utilizing the LIG-based bioelectrode. Because the prepared bioelectrodes are designed for monitoring biopotentials mounted on the target body regions, conformal contact and secured integration onto the body tissues is important without sacrificing electrical function, thereby, post-assembly processes were also designed; we will discuss the specific procedures next section.

Figure 1b illustrates the magnified view of the laser-scribed graphene film formation with porous microstructure on the LCP substrate. In the optical setup, the UV laser (beam diameter: ≈ 1 mm) scanned the surface of the exposed substrate by motorized step intervals (≈ 50 μm) along the x - and y -axis by the programmed input. Similar to other LIG processes, when a UV laser beam is directly irradiated onto the LCP surface, a rapid heat accumulation can be expected at the interface of the focused beam spot/LCP film, temporarily reaching local temperatures of up to ≈ 1000 $^{\circ}\text{C}$. This photo-induced thermal reaction transforms the polymeric source material (i.e., LCP film) to graphitic carbon only on the exposed area. In our custom-made optical system, the size of the laser beam spot (≈ 250 μm) exceeded the step interval (≈ 50 μm) which generally led to overlapped laser scanning results. Thus, only the limited resolution was correlated in the layout of the designed circuits and dimensional mismatches. However, to overcome this experimental condition, our approaches of protective metal shadow masking and mechanically predefined-cut LCP films were fully utilized, as depicted in Figure 1a. At this stage, we performed thermogravimetric-analysis (TGA) measurements at the temperature range from 28 to 700 $^{\circ}\text{C}$ and a heating rate of 10 $^{\circ}\text{C min}^{-1}$ under air and N_2 atmosphere to confirm the laser-induced carbonization of LCP film. As plotted in Figure S1, Supporting Information, there are two weight loss steps during the thermal decomposition processes under the air atmosphere (i.e., real experimental condition), whereas only one step was found in the N_2 atmospheric case. It is easy to understand that the thermal degradation mechanisms for the air condition at each stage generally involved interactions with oxygen molecules by the formation of CO and CO_2 , directly compared to the N_2 atmosphere. At the early stage of the thermal degradation process

(i.e., 470–510 $^{\circ}\text{C}$), the evaporated CO came from the terminal CO groups based on the molecular structure of LCP film, but oxygen molecules interacted with the decomposed crosslinking end groups at the second step (i.e., 530–600 $^{\circ}\text{C}$). Thus, no residue was left in the air atmosphere after TGA analysis, while the weight loss was found only 40% in the N_2 atmosphere case. Therefore, the UV laser irradiation was sufficient to provide the localized photo-thermal reaction of more than ≈ 500 $^{\circ}\text{C}$ for breaking the C–O and C=O bonds in the molecular structures of the LCP film, in which the remaining carbon precursor could be rearranged to form graphitic structures simultaneously with gas molecule generation.

To demonstrate programmed UV laser writing under ambient conditions on the LCP film, a complicated layout was designed and generated on a large scale for a flexible electronic circuit-enabled LIG substrate, as presented in Figure 1c (Figure S2a–d, Supporting Information); the digital photographs show black and white contrast, exhibiting the LIG-structured circuit arrays and the unexposed LCP film background (white). In the programmed UV laser writing process, the minimum resolution for line width and pitch was measured to be ≈ 130 μm and ≈ 300 μm , respectively. A simple example of the flexibility of the 25 μm -thick LIG/LCP circuit substrate was captured in the inset image in Figure 1d, conformally wrapping the half surface area of forearms. To observe the surface morphology of the LIG, we used scanning electron microscopy (SEM) as shown in Figure 1e, where the mesoporous graphene structure was successfully crafted with randomly distributed pore sizes, ranging from ≈ 200 nm to ≈ 2.2 μm . This porous structure was spontaneously produced due to the rapid exhale of gaseous products (i.e., CO and CO_2) by the photo-induced thermal reaction and residual carbon rearrangement from the surface of LCP film during the laser beam irradiation. This observation is consistent with other results from the LIG processes using carbon source materials such as PI, PEEK, wood, and cellulose.^[31–34] Interestingly, as shown in the inset, the cross-sectional view from the SEM image indicates that the 25 μm -thick LCP film was transformed into the overlying networked LIG layer (≈ 30 μm) with a residual layer of LCP film. Subsequently, the surface chemical properties and composition of the porous structured graphene were characterized by X-ray photoelectron spectroscopy (XPS) and elemental mapping analysis. In Figure S3, Supporting Information, the XPS survey spectra for LCP and LIG/LCP films reveal the binding energies of C 1s and O 1s for the surface chemical state from each sample, which was collected to be 284.8 and 532.6 eV, respectively. As the laser-induced carbonization of LCP film progressed, the intensity of the C 1s peak increased and the O 1s peak decreased, similar to other previous reports.^[35] The additional high-resolution C1s spectra of LIG/LCP film indicate that the LIG surface exhibits sp^2 carbons with a C–C/C=C peak prominently dominant at 284.8 eV, compared to the result of LCP film. Energy dispersive spectroscopy (EDS) was further used to measure the change of the carbon fraction after the laser irradiation on the LCP film, which results indicate the increased atomic ratio of carbon from $\approx 76\%$ (LCP film) to 96% (LIG/LCP film), as shown in Figure S4, Supporting Information.

Based on this information, we optimized the electrical conductivity for the LIG-based electrodes by slightly tuning laser

irradiation parameters, such as laser power and the number of scans over the same exposed area. As displayed in Figure 1e, the electrical conductivity was measured and qualified according to the laser power with the number of scans. At the first laser beam irradiation, it was found that the increased laser power was a dominant factor that affects the electrical conductivity (i.e., the sheet resistance) due to the sufficient amount of energy transfer to the LCP film; a higher laser power range efficiently carbonized the local surface of the LCP film, resulting in lower sheet resistance by sufficient photo-thermal effect. However, from the second time scanning, the sheet resistance was markedly reduced for all samples, as seen in the graph. It should be noted that the extended carbonization with multiple laser exposure guarantees high electrical performance due to the expansion of the LIG thickness with higher quality, but less correlated to the laser power. As previously reported, it is obviously acceptable that increasing laser power and multiple irradiation are general methods to obtain qualified electrical performance of LIG electrodes with reasonable sheet resistance.^[36] However, there is a trade-off in this parametric condition to maintain the flexibility and mechanical stability of the LIG-structured films because the excessive laser power and multiple irradiation generally cause partial damage to the carbon source substrates that substantially affect its mechanical properties.^[37] Therefore, it is important to balance the flexibility and mechanical stability of the electrically high-performance LIG electrodes by optimizing the physical parameters without the loss of intrinsic properties of the LCP film. On this, for clear guidance, we evaluated the correlation between the mechanical stability and the laser scanning passes by measuring the mechanical properties of LIG-structured films as a function of the number of laser scans at a typical power of 2.25 W, as presented in Figure S5, Supporting Information. A set of stress–strain curves exhibited a decreased trend of the measured tensile strength from ≈ 82.3 to ≈ 22.3 MPa, depending on the laser scan numbers. The LIG-structured films prepared by subsequent laser scans induced additional interaction with the LCP film and effective carbonization (i.e., increased conductivity), but the intrinsic mechanical strength was proportionally decreased with the degree of localized degradation of the LCP film. Note that, more than 5-time laser irradiation at the same location on the LCP film exhibited apparent deterioration of LIG/LCP film with the morphological changes in shape. In addition, the quality of the LIG produced on LCP film was qualified as a function of a number of scans at a specific laser power (2.25 W), using Raman spectroscopy (Figure 1f,g). As measured, three characteristic peaks for all samples were detected at ≈ 1339 , ≈ 1578 , and ≈ 2690 cm^{-1} , corresponding to D, G, and 2D peaks, respectively. Typical multilayer graphene peaks were observed from the collected spectra based on the intensity ratio of G to 2D peaks ($I_G/I_{2D} \approx 1.2$ – 1.4), in which the most intense G peaks for vibrational modes of the sp^2 carbon-carbon bonds with 2D peaks represent the graphitic lattice.^[38,39] In addition, the I_D/I_G can be used to estimate the relative crystalline quality of the LIG because the level of the D peak indicates a disordered state of the structure as the increased defect density. In Figure 1g, the quality of the LIG material was improved as the defect density decreased over multiple laser scanning passes, with a gradual decrease in I_D/I_G up to ≈ 0.58 due to the relatively low defect density.

2.2. Transfer Printing Process of Large-Scale LIG-Based Electrodes with Resolution Enhancement

The LIG-based electrodes, produced either by direct writing or microscale shadow masking on a 25 μm -thick LCP film, can serve as electrical pathways for interconnections that are readily integrated with other device components for practical applications. Further, in some cases, it can also be integrated into LIG-based conductive circuits by utilizing different types of substrates for each purpose, depending on the desired applications. As for this approach, the transfer printing technique into transparent or elastomeric substrates may provide one solution to expand their capabilities as a functional unit on desired target surfaces, such as curved areas.^[40] Hence, conformal contact adhesion to receiving surfaces of the substrates is a key parameter in physically stable interconnection and operation, integrated into the LIG-based circuit arrays. In addition, the transferred LIG electrodes must maintain their performance in a reconfigurable stacking arrangement while allowing clear separation due to mechanical mismatch between the underlying LCP film and the LIG electrodes. In this study, we schemed a dry transfer printing process to avoid the limitations of the traditionally used aqueous medium-based techniques, such as extended etching time and shape distortion caused by wet etching of the sacrificial layer, which may cause disordered fixation on the target substrate by generating unwanted defect regions, such as wrinkles.^[41,42]

As shown in Figure 2a, we demonstrated a simple technique for the transfer printing process of an array of example LIG electrodes (8×8 array: 64 in total) onto a polyethylene terephthalate (PET) film on a large scale, utilizing a customized roll-to-plate apparatus.^[43] An initially fabricated LIG-based electrode array formed on the LCP film was wrapped around a quartz roll (Young's modulus ≈ 70 GPa, diameter: 100 mm, right panels in Figure 2a), and then mounted on the moving stage. As schematically illustrated in Figure 2b, during the control of the bottom stage moving at a speed ($100 \mu\text{m s}^{-1}$), a firmly fixed adhesive-coated transparent PET film entirely transferred the LIG electrodes located on the LCP film with an optimized pressure (0.5 MPa) from the roll by continuously providing a localized conformal contact area. The optimized roll pressure was determined by the electrical conductivity of the transferred LIG electrode under the engaged range of pressure from 0.1 to 0.5 MPa (i.e., the maximum pressure in our experimental setup). As shown in Figure S6, Supporting Information, the level of the sheet resistance on the LIG-based electrodes was gradually decreased with increased roll pressure, indicating an improved performance of LIG transferred on the provided PET substrate. Accordingly, facilitating a uniform pressure distribution from the roll-to-plate geometry, a flexible carbon-based electrode array on a PET film ($t \approx 100 \mu\text{m}$) was successfully produced with a high yield, as captured in Figure 2c. After the roll-based dry transfer printing process, the surface of the transferred LIG and mother substrate was observed by SEM to confirm the changes in the morphological features with respect to the relatively high pressure and interactions with the adhesive film (Figure S7, Supporting Information). As expected, the residual LIG was left behind on the mother substrate in its original patterned shape by the physical separation, but the porous surface structure of the transferred LIG revealed a uniform film; clear contrast obviously indicates the boundary be-

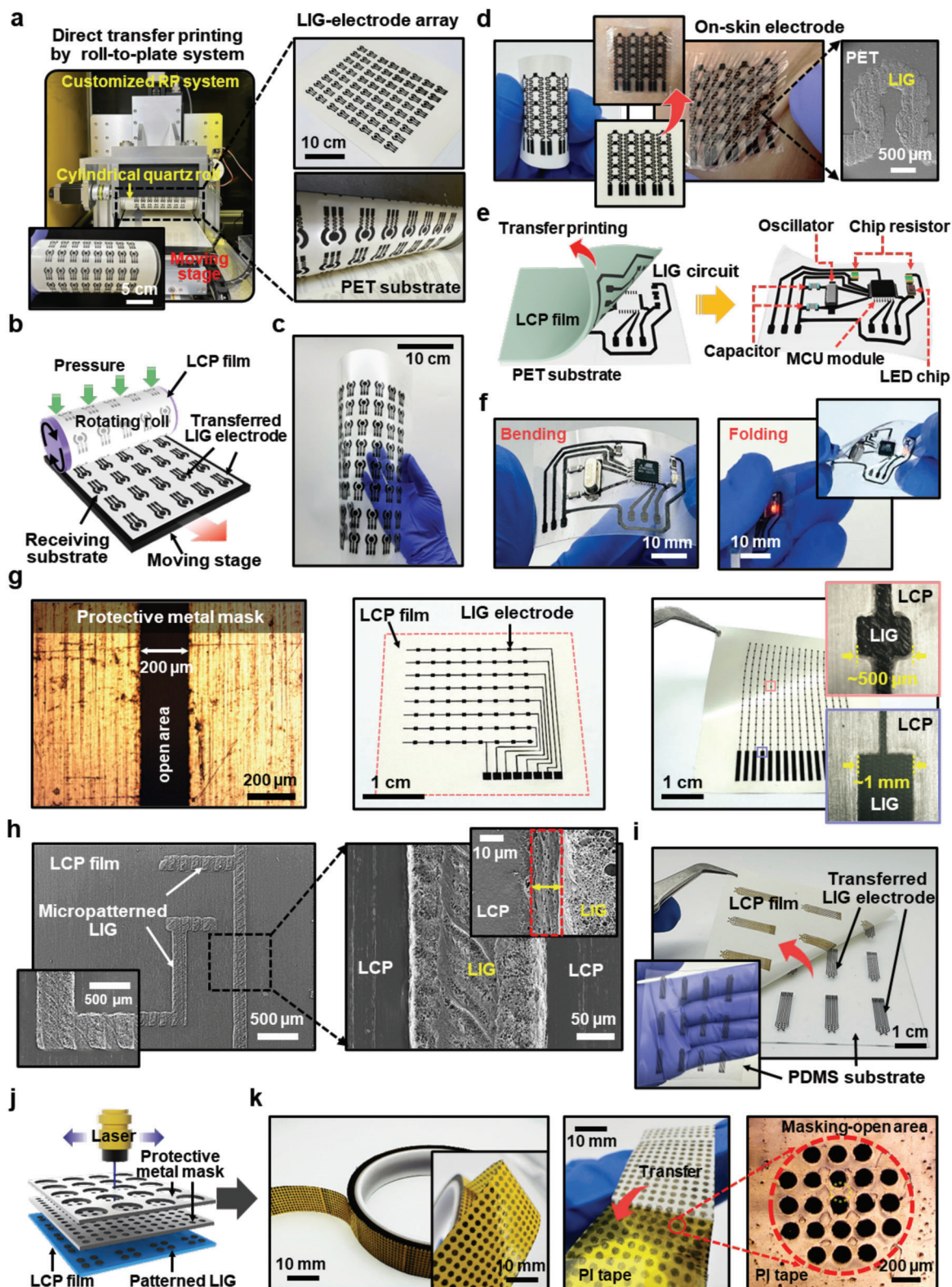


Figure 2. a) Photograph of the experimental setup of a roll-to-plate (RP) system for transfer printing of LIG electrodes onto a target PET substrate (right images: the patterned LIG electrode array (upper) and wrapped around a cylindrical quartz roll (lower)). b) Schematic of transfer print of LIG electrode array by using the RP system. c) Photograph of the transferred LIG electrode array on a flexible substrate. d) A skin-attachable LIG electrode with a serpentine-shaped design formed on LCP film (left), attached to the skin after peeling off from the carrier substrate (middle), and magnified SEM image of the serpentine-shaped LIG electrode (right). e, f) The transfer print of the LIG-based flexible circuit array and SMT integration with SMD modules,

tween the transferred LIG pattern and the adhesive layer of PET film (Figure S7a, Supporting Information). Moreover, compared with the pristine LIG structure (Figure 1d), the thickness level of the LIG was slightly reduced from ≈ 50 to ≈ 40 μm (i.e., residual LIG layer of $\approx 20\%$), as presented in Figure S7b, Supporting Information. Due to this residual LIG left behind on the LCP film, a decrease in conductivity was measured from the LIG transferred to the PET substrate compared to the originally produced LIG/LCP film (Figure S7c, Supporting Information). While this may be an issue that can be solved with other transfer printing methods, our proposed roll-to-plate transfer process can be useful to provide a new option from the point of view of large-scale manufacturing tools. As an extended concept, for example, we demonstrated wearable bioelectrodes featuring a tattoo-like thin film in skin-attachable form.^[44] In Figure 2d and Figure S8, Supporting Information, a design and series of transfer printing processes were presented for crafting the LIG-based electronic tattoo, in which a layout of a serpentine-shaped structure was adopted to maintain stable conductivity of the electrical channels from the local elastic deformation. The digital photographs show an array of flexible LIG-based bioelectrodes, consisting of a working electrode (2×2 mm^2) on the LCP film with separately connected electrodes with a ≈ 500 μm -width. In this configured circuit, a monolithically arranged LIG-based electrode array was transferred to the skin surface using a bilayered adhesive film (optical clear adhesive, OCA film, $t \approx 5$ μm)/guide PET film ($t \approx 50$ μm), which was conformally attached to the back of the hand by the removal of the PET guide film; the middle and right panels in Figure 2d represent on-skin bioelectrode and an magnified view of SEM image on a circular-shaped LIG electrode.

To demonstrate the compatibility of the scalable transfer-printed electrode array with the surface mount technology (SMT),^[45] we developed a straightforward electronic circuit, as shown in Figure 2e. In the configured circuit array (Figure S9, Supporting Information), we carefully designed the traces and pads to ensure the stable physical contact and operation of arranged electronic components. We matched the pad size and electrical characteristics of the integrated circuits (e.g., resistance) for the selected suitable SMD components, mounted on the flexible circuit board with the patterned LIG/PET substrate ($t = 50$ μm). Specifically, LED chip, resistors, oscillator, capacitors, and microcontroller unit (MCU) modules were positioned and connected to the electrical pads using solder paste. The MCU provided precise control over LED operation by programming logic sets through input/output (Digital I/O) pins, executing user-defined codes, with additional chip resistors that governed the current flow to the LED in the circuit. Notably, to determine the execution speed and the frequency of the MCU, a standard crystal oscillator (16.000 MHz) was also incorporated to regulate the timing and synchronization required for LED element operation, for which capacitors were equipped to ensure stability and main-

tain the accuracy and desired frequency of the clock signals. The digital image in Figure 2f displays the integration of the SMDs on the LIG-based circuit board, capable of controlling the blinking time through the MCU and oscillator, during the operating LED chip in a folded state. As demonstrated in the Supporting Movie S1, Supporting Information, this simple circuit design utilized the general-purpose input/output pin of the MCU to execute digital values (0 or 1) in output mode by setting the voltage as high (1) or low (0) to adjust the operating cycles. Consequently, the gradual blinking of LED elements could be operated through programming functions; by gradually reducing the set timer value from 500 to 50 ms, the LED's blinking speed became faster, and when the timer value returned to the initial set value, the LED resumed its repeated operation. It is worth noting that this solid and electrically stable circuit connection was achieved by filling the gap between each surface-mounted component and the pad area of the LIG circuit with additional underfill and PDMS encapsulant, which enhanced the mechanical stability between rigid electronic components and flexible LIG circuit. Thus, the LED-equipped flexible LIG circuit could be operated under bending or slightly twisted deformations (inset in Figure 2f). This simple example of the performance of multiple SMD components highlights the potential to utilize a large-scale flexible circuit based on LIG electrodes, consisting of complex trace configurations, without impairing the function of electronic components.

In our experimental condition, the resolution of the generated LIG patterns through direct writing was fundamentally limited by the size of the focused laser spot, which is highly dependent on the optical operating system. Therefore, to enhance resolution in pattern generation, we combined a laser exposure system and a stencil masking process that has the potential to expand the application range for controlling definition in circuit arrays beyond the direct writing for patterned LIG electrodes. Microscale stencil lithography using shadow masking has been introduced to transfer micropatterns to target substrates without the use of a photoresist, enabling surface patterning of functional materials with low mechanical rigidity, as well as simplifying the process, reducing manufacturing costs, and providing reusability. Figure 2g,h illustrates various examples of LIG pattern transfers using shadow masks, which depict a sophisticated LIG electrode array achieved by laser scanning over the protective shadow masks in physical contact with the LCP film. The generated LIG electrodes from this method exhibited excellent controllability in sharp contrast particularly at the extremity of the laser-exposed area on the LCP surface, as presented in the middle and right panels of Figure 2g. Notably, SEM images in Figure 2h show the representative patterned surface of the LIG electrode with a magnified view, revealing a clear boundary at the laser-exposed area (right inset in Figure 2h). Additional examples in Figure S10, Supporting Information, demonstrate the apparent resolution obtained by applying the shadow mask on

including MCU to operate the blinking LED chip. g) Optical micrograph of the protective metal mask for selective laser transmission through the open area (left), and photographs of the LIG electrodes crafted on the LCP film (inset: optical micrographs of 1:1 resolution by the shadow mask). h) SEM images of the resolution-improved LIG electrodes with sharp contrast at the edges. i) Photograph of the transfer-printed LIG electrode array on the elastomeric PDMS substrate (inset: transferred LIG electrode on a large scale). j) Schematic of stacking shadow masks for versatile designing of the patterned LIG films. k) The representative photographs of transfer-printed LIG patterns manufactured by double-stacked shadow masks for an array of circular islands with different diameters.

the LCP film. This approach successfully crafted line-spacing patterns (200 μm in width) and isolated circular-shaped island arrays (100 μm in diameter) over a large area on the laser-protected LCP films. As measured, the shadow masking method resulted in only a slight variation from the initially provided mask size, even with multiple laser exposures (less than 10%), compared to the direct writing of UV laser (Figure S11, Supporting Information). Furthermore, when the substrate was replaced with commonly used PI film, the shadow masking method produced a LIG electrode array, with magnified SEM images confirming the generation of 1:1 micropatterns with the circular-shaped electrodes (Figure S12a,b, Supporting Information). For more information, a direct comparison of the electrical conductivity showed that the sheet resistance of the LIG formed on the PI film was comparable to that of the LCP film under the same laser exposure conditions, as presented in Figure S12c, Supporting Information. Interestingly, as the laser-induced carbonization proceeded consecutively with 3-time or more laser scan passes, the level of the sheet resistance overlapped at a similar range regardless of the source material (Figure S12c, Supporting Information). As appeared in Figure 2i, this LIG electrode array (4×3 array) could be transferred by a peeling-off process with the elastomeric material (i.e., PDMS). As an additional stencil masking approach, Figure 2j and Figure S13, Supporting Information, present schematic diagrams illustrating the process of manufacturing LIG by laminating the metal masks. These results show various designs of LIG patterns achieved by simply rotating angles of the overlapping shadow masks, creating line patterns with pitches of ≈ 200 μm and ≈ 400 μm at 0° , 45° , and 90° . The use of overlapping shadow masks offers significant advantages in terms of reducing the processing time required for designing simple repetitive micropatterns with various shapes. Further, the alignment of the shadow mask is the sole controllable variable for manufacturing elaborate patterns of LIG, leading to improved resolution up to ≈ 70 μm . Figure 2k provides a representative example of this approach, depicting the LIG fabricated utilizing two shadow masks to create a circular-pattern array with different diameters over the surface area, transferred to PI adhesive tape. The combination of shadow masking techniques with specific shapes holds the potential for increasing productivity by reducing the processing time of the manufacturing process, which can be widely used in other fields, including tissue engineering, biomedical devices, flexible electronics, and wearable sensors.^[46–48]

2.3. Body-Attachable LIG-Based Electrodes for Health Monitoring and Biochemical Sensor Applications

Figure 3a illustrates a developed design of the LIG-based bioelectrode, which can be transformed into the shape of the skin to measure electrophysiological signals, such as ECG and EMG. Because it is crucial for wearable bioelectrodes to maintain conductivity during biaxial stretching to acquire electrophysiological signals on the surface of human skin, a mechanically deformable form of design may be a key factor in the body-attachable bioelectrodes.^[49] In our strategy, an example of kirigami configuration was adapted to transform a non-stretchable sheet of LIG electrodes into a highly stretchable structure, accommodating large tensile strains applied by out-of-plane strain to reduce

the local resistance of the sheet. As illustrated in Figure 3b, we schemed kirigami building blocks in closed and open configurations (i.e., bistable auxetic structure), consisting of three intersecting lines overlapping equilateral elements within a triangular unit that act primarily as rigid bodies with pointwise hinges (black dots) and connected rotating and stationary elements (colored yellow and green, respectively). Thus, according to the applied strain, the rotating unit revolves while connected to the living hinges, and the flexible hinges can be bent to provide geometrical constraints by the uniform deformation. Thus, it can be easily transformed through the rotation mechanism of a structure, such as a deployable or foldable structure, according to the natural deformity of the skin, making it suitable for use as a bioelectrode. In fact, within a defined layout in Figure 3b, the operating condition in the kirigami structure depends on several parameters, including the geometric configuration of the cut, the degree of elongation imposed, and the stiffness of the constituent materials.^[50] As recently reported, these parameters play a crucial role in determining structural stability, which suggests that the mechanical behavior of the triangular bistable auxetics type of kirigami structure utilized in the study can be influenced by specific geometric parameters, such as the relationship between the hinge thickness (t/L) and the rotation unit width (a/L). Therefore, the ratio of the local minimum strain energy (E_{min}) in the deformed stable state of the structure to the strain energy barrier (E_{max}), denoted as η , can be defined to assess the mechanical stability.^[51] In our experimental approach, it was postulated that the proposed auxetic configuration exhibited structural bistability (i.e., $\eta < 1$) under the operating conditions of $t/L = 0.045$ and $a/L = 0.5$; the expected range of η was to be ≈ 0.4 – 0.5 , indicating bistability. Based on this configuration, a backing layer of 50 μm -thick adhesive-coated PET film was laminated to support the mechanical stability of the LIG electrode created on a thin LCP film (25 μm), and then the UV laser irradiation was applied to the whole surface of the exposed LCP film. As a final step, a programmed mechanical cutting was processed to tailor the designed auxetic structure, producing kirigami structured electrical pads in a stretchable format. In the following, conductive hydrogel was applied to the surface of the layered electrodes to exert conformal contact between the LIG electrode and the skin (Figure 3c). As presented in Figure 3d,e, the mechanical and electrical stability of the kirigami-inspired LIG bioelectrodes was evaluated using a biaxial test stage to examine the resistance changes by pulling both edges until the electrode structure was fully extended. As appeared in Figure 3d, the flexible hinges inside the kirigami structured LIG electrode mechanically connect adjacent rigid rotating units (i.e., three-cut motif elements) up to $\approx 57\%$ biaxial stretch at the same angle in opposite directions, indicating the identical strain in both x and y directions (Movie S2, Supporting Information). However, the resistance changes were observed after the biaxial stretching due to the local mechanical degradation of the hinges starting from the higher strain range of $\approx 35.7\%$ (Figure 3e). In addition, as shown in Figure 3f, under the repetitive strain, the changes of R/R_0 were measured with large deformation of the electrodes by the rotating of the connected regions during 1000 cycles of biaxial stretching, in which the range of resistance changes further increased when the degree of plastic deformation became severe. A reasonable operating range of the kirigami-based LIG electrode was confirmed with stable conduc-

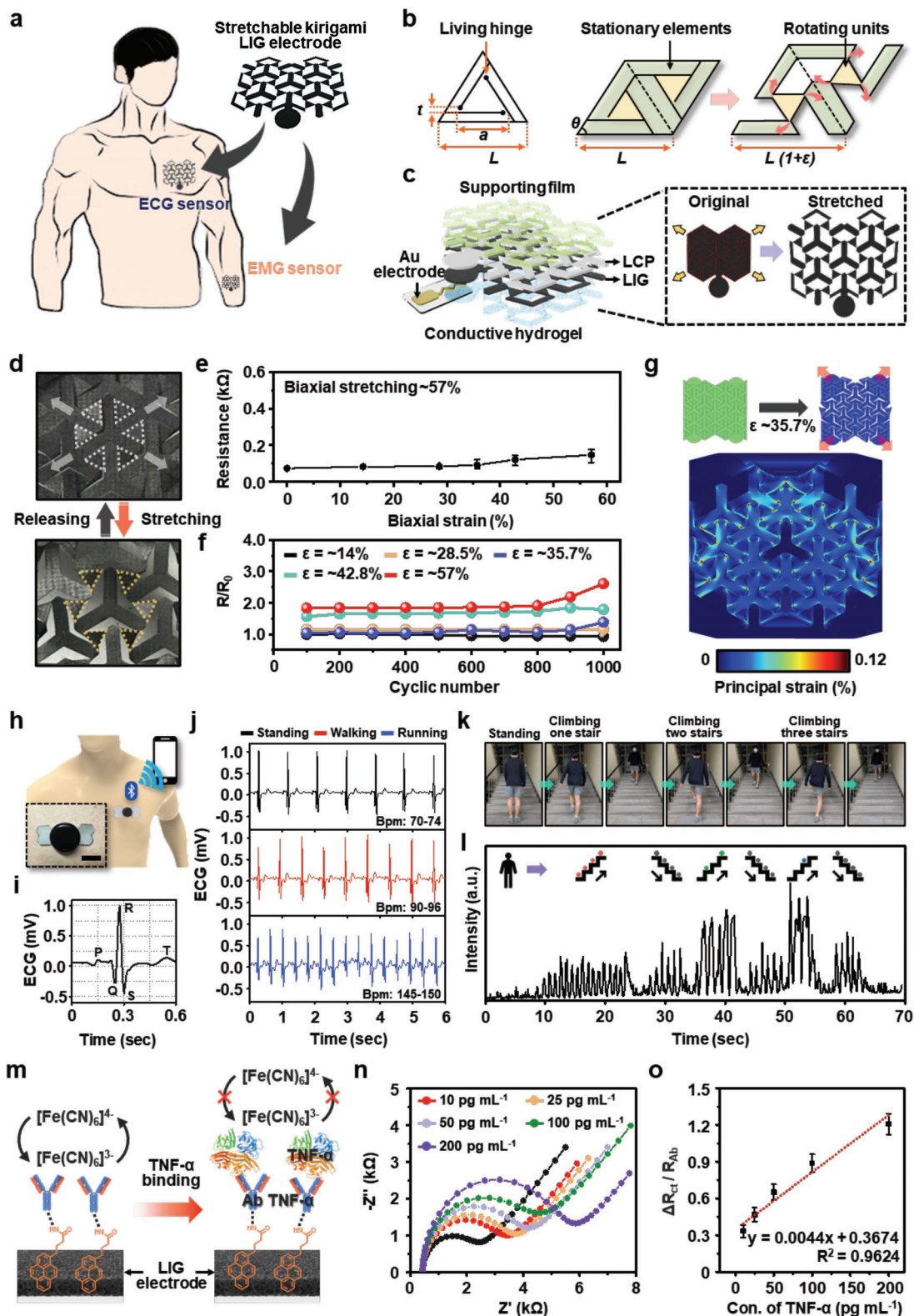


Figure 3. a) Schematic illustration of body-attachable LIG-based electrodes for monitoring electrophysiological signals of EMG and ECG. b) Diagrams of the kirigami design as a body-attachable bioelectrode with high stretchability and electrical stability operated by rotating triangular units and living hinges. c) Schematic of structured layers of body-attachable LIG-based bioelectrode in a stretched form. d) Digital images of the initial and biaxially stretched state of the kirigami-inspired LIG electrode (lower: 57% biaxial stretching). e) The resistance changes of kirigami LIG-electrodes according to the level of biaxial stretching up to 57% ($n = 5$). f) The normalized resistance changes of kirigami-based electrodes as a function of the engaged

tivity under the stretching conditions of $\approx 35.7\%$ strain for 1000 cycles. To gain further insights into the observed mechanical phenomena, the geometrical model with switchable units in the kirigami pattern was also computed using finite element analysis (FEA) by evaluating the parametric conditions of the mechanical deformation. In the virtually assumed operating state on the bistable structure (6×6 triangular units: 36 in total), Figure 3g illustrates the distributions of principal strain under the stable state of the kirigami structure ($\epsilon \approx 35.7\%$) with the maximum local strains of 0.747 at the point of the living hinges (upper area in the asymmetric configuration). Moreover, additional FEA analyses were conducted to examine other deformed states, as depicted in Figure S14, Supporting Information. These analyses revealed that stress was primarily concentrated in the hinge regions, while the rest of the structure exhibited negligible strain. Considering the resolution limit of the currently available strategy, the LIG-based electrodes were optimized particularly for reversible mechanical performance. This is because the maximum local strain of the kirigami structure under isotropic biaxial strain ($\approx 1.25\%$ at $\epsilon \approx 57\%$) is considerably lower than the strain level ($\approx 2.3\%$) required to break the LCP film.^[52] However, the compliant living hinges might experience crack propagation in the repeated iso-biaxial deformation process when strain exceeding $\approx 35.7\%$ was applied (Figure 3f). Therefore, within certain experimental conditions of strain levels, the high structural stability of the kirigami design can secure the necessary elasticity for the purpose of acquiring electrophysiological signals on the skin by the efficient in-plane transformation of opening and closure.

To practically use the kirigami structured LIG bioelectrode, we collected biometric information from the human body by facilitating ECG and EMG modules that can monitor physical health or diagnose diseases. Figure 3h shows a wireless ECG module connected to a patch-type kirigami LIG bioelectrode, attached to the chest skin for real-time monitoring. A pair of LIG bioelectrodes coupled with an ECG module could continuously transfer heart-beating signals to a mobile phone for biosignal acquisition with a contact area of $\approx 471.6 \text{ mm}^2$ with hydrogel between the electrode's interface and the skin. Figure 3i displays the electrical activity generated by a typical single heartbeat measured in a resting state, appearing with almost no noise representing classified P, QRS, and T wave shapes.^[53] Next, to test the performance of the LIG bioelectrode according to body movement, ECG signal changes were measured in three behavioral motions such as standing, walking, and running, as shown in Figure 3j. The R–R interval (corresponding to the time between two consecutive R peaks) in a standing state was to be 850 ms, from which a heart rate of 70–74 bpm was estimated. The duration of the QRS wave was less than 0.1 s, and the time interval between the Q and T waves fell below the 0.4 s limit. As the exercise phase increased,

the R–R interval decreased from 660 ms (walking) to 410 ms (running), and the heart rate was recorded as 90–95 bpm (walking) and 145–150 bpm (running), respectively. The measured ECG signals not only collected an accurate heart rate in real-time but also provided cardiovascular information such as the depolarization state (QRS complex) by the left and right ventricles of the cardiac wave, making it possible to use in diagnosing cardiovascular diseases. From these features, we inferred that the recorded signals using kirigami-based LIG bioelectrode were verified as all the referenced features and the duration of the wave. As another example of the application, performance tests were conducted to obtain EMG signals induced by quasi-periodic electrical signals generated through muscle contraction activity, using LIG-based bioelectrodes. The wireless EMG sensing module for evaluating muscle contraction and relaxation was equipped with three LIG-based bioelectrodes, as shown in Figure S15a, Supporting Information. To collect EMG signals based on the contraction/relaxation state of the calf muscle, the ability to climb stairs was monitored by attaching the LIG bioelectrodes to the calf muscle of the right leg (Figure 3k). Figure 3l illustrates the changes in the measured EMG signal intensity as per the intensity of climbing the stairs. The number of steps climbed on stairs arranged at regular intervals and heights represented the stimulation applied to the muscles with a 5 s break before/after climbing the stairs completely. As a result, the EMG signal strength increased when the right leg supported the ground, and the stronger the exercise stimulus, the stronger the EMG signal strength further increased (Figure 3l; Movie S3, Supporting Information). It was confirmed that the load imposed on the muscles of the right leg was maintained constant during the process of descending the stairs one by one after each step; the number of dots in the inset graph represents the number of stairs moved at one time. For more measurements to check whether the load applied to the calf muscle of the right leg affected the movement of the muscle of the left leg, running in place at a constant height was performed to reflect EMG signal changes, as presented in Figure S15b, Supporting Information. The intensity of the EMG signal increased when the left leg was used to jump in place with the right leg floating, whereas the EMG signal intensity was hardly affected in the opposite case. In addition, when jumping in place using both legs, the load on the right calf muscle was reduced, and the strength of the EMG signal was halved (Figure S15b, Supporting Information). As demonstrated, the LIG-based bioelectrodes introduced a kirigami design to provide high deformability for elongation, bending, and twisting, allowing for conformal integration of skin-like electrodes with high performance.

We extended our approach to an electrochemical biosensor using the LIG-based electrode capable of detecting biomolecule, TNF- α (tumor necrosis factor α), which existed in biological sam-

strain levels during 1000 cycles of biaxial stretching. g) An image of computed FEA on the principal strain distribution of the asymmetrically arranged kirigami electrode at the biaxial strain of 35.7%. h) Schematic and photograph (inset) of the skin-attached kirigami structured electrical pads connected to a wireless ECG module. i) Real-time recorded ECG signal by using kirigami LIG bioelectrode during a resting state. j) Monitoring of the ECG signals collected from three different behavioral motions (standing, walking, and running), conforming high stability of the LIG bioelectrodes. k,l) Photograph of going up and down stairs to demonstrate the LIG patch-type electrode, connected to the EMG module, by recording the contraction/relaxation state from a calf muscle. m) Schematic on the electrochemical sensing mechanism of LIG-based biosensor to detect TNF- α protein. n) EIS responses of the Ab-loaded LIG-based biosensors for evaluating different concentrations of TNF- α . o) The linear relationship between $\Delta R_{ct}/R_{Ab}$ values and the applied concentration range of the TNF- α for extracting LOD and LOQ ($n = 3$).

ples such as serum and saliva. TNF- α is a pro-inflammatory cytokine secreted by activated macrophages that are known to increase when the inflammatory cascade is activated, contributing to diseases like rheumatoid arthritis, neurodegenerative diseases, diabetes, stroke, and HIV.^[54] TNF- α is a critical biomarker for inflammatory diseases such as infection, heart failure, and leukemia. Its concentration in most healthy individuals is less than 10 pg mL⁻¹, whereas over 80% of patients with severe autoimmune diseases have levels between 10 and 300 pg mL⁻¹.^[55] In saliva, the salivary concentration of TNF- α is about 30 pg mL⁻¹ in oral cancer patients and 3 pg mL⁻¹ in healthy individuals.^[56] Simply fabricated LIG-based three terminal electrodes, transferred on PET film (Figure 2a), were utilized to detect TNF- α as an immunosensor that has high accuracy and precision since the porous LIG has a large surface area with a fast electron transfer rate. The preparation of the LIG-based electrochemical biosensor involved surface modification of LIG, antibody immobilization, and subsequent protein deposition. The working electrode (WE) has a diameter of 8 mm, and the end of the WE maintained constant contact with the redox solution during electrochemical sensing, achieved through passivation. Next, 1-pyrenebutyric acid (1-PBA) was immobilized on the LIG surface through π - π stacking and hydrophobic interactions. TNF- α antibody (Ab-TNF- α) was then covalently coupled using EDC/NHS, and unreacted activated groups were blocked with BSA; this step ensured the specific binding ability to the TNF- α protein. Therefore, the LIG/1-PBA/NHS-EDC/Ab-TNF- α /BSA biosensor could detect TNF- α protein sensitively without a label. To evaluate the electrochemical performance of the biosensor, electrochemical impedance spectroscopy (EIS) was performed using 10 mM K₄[Fe(CN)₆]^{3-/4-} under the conditions of a frequency range of 0.05–100 kHz, a potential of 0.2 V, and an amplitude of 10 mV. Because the EIS is a highly sensitive technique for monitoring the impedance fluctuations of biosensors, the result can provide information on the interfacial characteristics between the electrode surface and the electrolyte solution, the adsorption process, and the interaction of biorecognition molecules with the WE surface. As presented in Figure 3m, the electrochemical sensing mechanism was illustrated in the surface-modified LIG-based biosensor by binding the standard TNF- α protein to the WE surface. As the mass of TNF- α bound to the Ab-TNF- α on the WE surface increases, the redox probe, K₄[Fe(CN)₆]^{3-/4-}, restricts diffusion to the electrode surface, increasing the semicircular diameter of the Nyquist plot. Figure 3n shows the LIG electrode-based biosensor's electrochemical detection capability, with a concentration-dependent impedance response to TNF- α protein. In this experiment, standard TNF- α solution (10 μ L) was diluted in various concentrations from 10 to 200 pg mL⁻¹ in PBS buffer dropped on the WE, and incubated for a few minutes to monitor the changes in R_{ct} values. The equivalent circuit model in EIS response includes the resistance of the electrolyte solution (R_s), the charge transfer resistance (R_{ct}), the double-layer capacitance related to the capacitance of the composite bioactive layer, and the Warburg impedance (Z_w) related to normal diffusion through the composite layer to the electrode surface (Figure 3n). As the concentration of TNF- α protein increased, the diameter of the semicircle (R_{ct}) in the Nyquist plot gradually increased, which suggests that the interaction between Ab-TNF- α and TNF- α protein on the surface of the WE may impede electron transport and increase the values

in R_{ct} . In the following, the EIS data was used to plot a calibration curve of the immunosensor with different TNF- α concentrations for the quantitative determination of the sensitivity and linear operating range of the electrochemical biosensor. Based on the measured results, the calibration plot of the LIG-based biosensor can be estimated using the equation, $\Delta R_{ct} = R_{ct}(\text{TNF-}\alpha) - R_{ct}(\text{Ab})$. Here, the $R_{ct}(\text{TNF-}\alpha)$ refers to the value of the semicircle diameter (i.e., charges of the transfer resistance) after the interaction between Ab-TNF- α and antigen TNF- α protein, and $R_{ct}(\text{Ab})$ refers to the semicircle diameter after the deposition of Ab-TNF- α through a series of binding processes and immobilization with BSA. The linear relationship between $\Delta R_{ct}/R_{ct}(\text{Ab})$ and concentration is shown in Figure 3o, indicating a linear range of 10–200 pg mL⁻¹ with a linear regression equation given by $y = 0.0044x + 0.3674$ and correlation of $R^2 = 0.962$. The limit of detection (LOD) and limit of quantification (LOQ) for TNF- α could be calculated using the relationship of $k \times S / m$, where S is the standard deviation of the y -intercept, and m is the slope of the calibration curve, corresponding to $k = 3.3$ for LOD and $k = 10$ for LOQ. Therefore, the LOD and LOQ values were estimated to be ≈ 9.32 pg mL⁻¹ and ≈ 28.2 pg mL⁻¹, respectively. Based on the EIS responses from the LIG-based biosensor, highly qualified performance might be due to the increased surface area resulting from the structural properties of the porous LIG, which implies that more antibodies can interact with the antigen protein by increasing the amount of the antibody bound to the WE surface.^[57]

2.4. LIG Bioelectrode-Based Neural Interface: Electrochemical Characteristics of Microelectrodes and In Vivo Applications

The LIG-based bioelectrode formed on the biocompatible LCP film was utilized for in vivo cortical recording and stimulation on the basis of its electrochemical properties and high flexibility (Figure S16, Supporting Information). In the cell viability tests, LIG films generated from LCP films were also verified to be sufficiently biocompatible substrates (Figure S17, Supporting Information). Figure 4a shows the LIG-generated bioelectrode array (6 \times 4: 24 in total) individually formed on an LCP substrate, which enables an 8-channel electrophysiological interface with the brain. The magnified view of the SEM images represents a desired sharp contrast of the LIG pattern with the help of metal shadow-making and subsequent laser irradiation (Figure 4b). As presented in Figure 4c, the LIG electrodes on the LCP substrate were encapsulated by another LCP cover layer with pre-defined opening windows in an LCP/LIG/LCP multilayered configuration, followed by the interconnection of the terminal pads to a flat ribbon cable using anisotropic conductive film (ACF) (Figure S18, Supporting Information). Homogeneous encapsulation, achieved by thermal diffusing lamination of the LCP-on-LCP film, is expected to provide superior durability for chronically implanted neuroprosthetics due to its low moisture absorption rate (i.e., <0.04%), compared to other biocompatible insulating materials, such as PI (i.e., $\approx 2.8\%$), PDMS (i.e., <1%), and parylene-C (i.e., 0.06–0.6%).^[23,58] Based on the previous reports, the long-term reliability of LCP encapsulation has been assessed through accelerated soak tests. For example, the LCP-encapsulated interdigitated patterns survived for more than 300 days by soaking in 75 °C PBS, significantly longer than parylene-

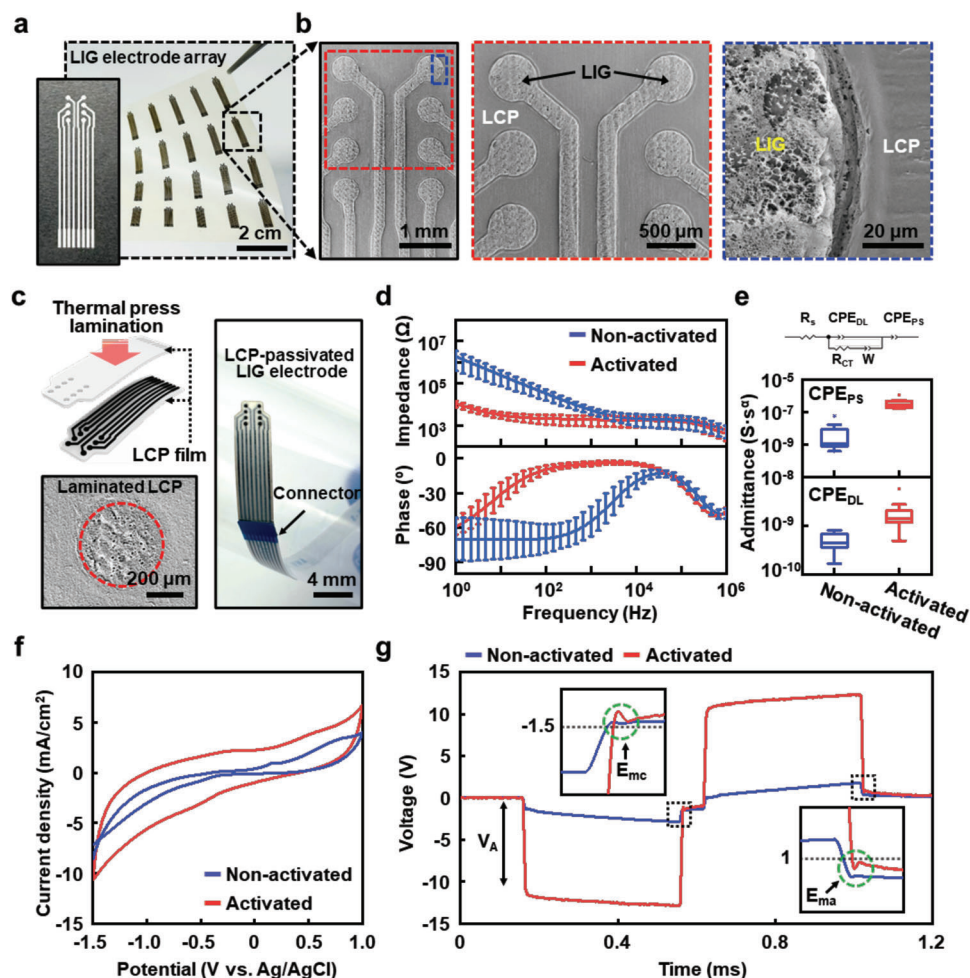


Figure 4. The LIG-based neural microelectrodes array and its electrochemical characterization. a) LIG-based microelectrode array manufactured by shadow masking with laser irradiation. b) SEM images of the surface of circular microelectrodes on LCP film; magnified SEM image shows clear contrast on the edge of the electrode. c) A schematic of homogeneous thermal diffusing lamination of LCP-based microelectrode array for encapsulation (8 channels), magnified SEM image of the circularly exposed electrode, and a digital image of LCP-passivated LIG neural interface electrically connected via an ACF film. d) Impedance spectrum of the LIG microelectrodes before/after the activation process ($n = 17$ for each group). e) EIS data fitted into the equivalent circuit model reveals an increase in the CPE values after the activation ($n = 17$ for each group). f) CV curves of the LIG microelectrodes before/after the activation process. g) Voltage transient of LIG microelectrodes under maximum current injection where E_{mc} or E_{ma} exceed the LIG water window.

C (i.e., 66 days) and polyimide (i.e., 117 days) encapsulation.^[30] Moreover, the LCP-based retinal electrode array maintained stable insulation for 114 days in saline solution at 87 °C,^[59] suggesting a potential lifetime of around 10 years at the body temperature.

Neural electrodes typically require specific electrochemical characteristics that vary depending on several factors, including the mode of interface (i.e., recording or stimulation), geometric parameters (i.e., size and shape), and types of signals (i.e., spike or field).^[60,61] In this study, the electrochemical activation process of LIG was developed to enhance or modulate the electrochemical properties for use in neural interfaces. The activation step involved repeated voltage scanning from -2 V to 1.5 V (vs Ag/AgCl) at a scan rate of 50 mV s⁻¹ in PBS solution.^[62,63] This resulted in a gradual expansion of the cyclic voltammery (CV) curves, reaching a saturation point after approximately 90

cycles, as shown in Figure S19, Supporting Information. The electrochemical properties of LIG electrodes were quantitatively analyzed before and after the activation process in terms of EIS with equivalent circuit models, cathodic charge storage capacity (CSC_C), and charge injection capacity (CIC). Figure 4d displays the EIS curves of the LIG electrodes, demonstrating the effectiveness of the activation process in reducing the impedance magnitudes within the frequency range up to 10 kHz. The activated LIG electrodes exhibited 69-fold and 2.8-fold lower mean impedance magnitudes at 1 Hz and 1 kHz, respectively, compared to those before activation.^[64] Additionally, the activation led to a transition of phase angles from predominantly capacitive (-90° to -40°) to resistive behavior (0° to -20°), consistent with the relative frequency-independent magnitudes of the activated LIG. The mechanism underlying the lowered impedance of the activated LIG was quantitatively and statistically inves-

tigated through an equivalent circuit model,^[65,66] as suggested in Figure 4e. We postulated that the primary factor responsible for the observed impedance change is the intercalation of electrolyte ions into the layers of LIG. The anions and cations present in PBS could be inserted between the graphene layers, potentially forming graphite intercalation compounds, as previously reported.^[67,68] Such intercalated ions between graphene layers are believed to expand the effective surface area of the activated LIG electrodes, facilitating the charge transfer through the pseudocapacitive behavior of the intercalated ions.^[63,69,70] These hypotheses were validated by the significantly increased values of two constant phase elements (CPE) after activation, as illustrated in Figure 4e, along with other circuit components (Figure S20, Supporting Information). During the activation step, the CPE_{PS}, representing the pseudocapacitance resulting from ion intercalation, experienced a notable increase of two orders of magnitude ($p < 0.001$). Similarly, the CPE_{DL} (i.e., double-layer capacitance) was increased by one order of magnitude ($p < 0.001$). Therefore, it can be speculated that the intercalation of ions and the resulting increase in CPE played a dominant role in enhancing the charge transfer process in the activated LIG.^[64] A good agreement between the measured EIS data and the fitted curves in Figure S21, Supporting Information, confirms successful fitting up to 1 MHz, both before and after the activation process. The outcomes obtained from the XPS and EDS analyses presented in Figures S22, S23, Supporting Information, reveal the presence of electrolyte ions, compared to the results of bare LCP film and pristine LIG (Figures S3, S4, Supporting Information), specifically Na⁺, Cl⁻, and K⁺, only within the activated LIG layer, providing additional support for the aforementioned hypothesis. In Figure 4f, the CV curves of the LIG electrodes demonstrate a significant enlargement of the enclosed area following the activation process. This results in an enhanced mean CSC_C, increasing from 21.2 to 118.1 mC cm⁻², which is higher than the CSC_C values of well-known high-performance neural interfacing materials such as iridium oxide (IrO_x), carbon-based materials, and conductive polymeric materials (refer to Table S1, Supporting Information, for more information). The CSC_C values were measured within a water window ranging from -1.5 V to 1 V for the LIG electrodes. It is noteworthy that carbon-based electrodes generally exhibit broader water windows compared to metallic electrodes, contributing to their higher CSC_C values.^[22] During the activation process, relevant redox peaks were observed at -2 V (water reduction), 1 V (oxygen reduction), and 1.5 V (water oxidation), consistent with previous reports (Figure S19, Supporting Information).^[71] The CIC of the LIG electrodes was evaluated from the voltage transient waveforms in response to increasing current injection in PBS, as shown in Figure 4g. The critical current amplitude (I_{\max}), beyond which the maximum cathodal or anodal excursion potential (E_{mc} or E_{ma}) exceeded the LIG water window, was translated into the maximum injectable charges per electrode area with a fixed pulse duration of 400 μs , as shown in the insets of Figure 4g.^[72] The activation process led to an 8.2-fold enhancement of the mean CIC, increasing from 0.17 to 1.4 mC cm⁻² (I_{\max} : 0.84 mA to 6.8 mA). Such a high CIC of LIG electrodes may secure safe and effective stimulation with a wide range of current levels without causing irreversible reactions, suggesting a broad dynamic range for various neural stimulating applications. So far, the above characterizations suggest

that the intercalation of ions facilitates the charge transfer process between the LIG and electrolyte, leading to notable improvements in electrochemical performance, as evidenced by reduced impedance levels and increased values of CSC_C and CIC. The long-term pulsing stability of the LIG electrodes was assessed in PBS by applying repeated current pulses at the maximum strength. The EIS, CSC_C, and CIC remained almost unchanged even after applying 5 million cycles (Figure S24a–d, Supporting Information). Additionally, the long-term stability of the LIG electrode in an aqueous physiological environment was evaluated through an accelerated soak test in PBS at 47 °C. The impedance curves remained stable for 14 days, which corresponds to approximately one month at body temperature (Figure S24e, Supporting Information).^[73] These soak tests in an accelerated condition with continued impedance measurement of the activated LIG electrodes collectively suggest the potential suitability of LIG electrodes for chronic applications. More importantly, the simple fabrication process of single-step laser scribing on the biocompatible LCP film, coupled with reliable LCP-on-LCP encapsulation, is to provide an attractive option for producing microelectrode arrays for neural interfacing. This approach eliminates the need for vacuum deposition and photolithography while featuring an excellent electrochemical performance with promising long-term durability for in vivo applications (Table S1, Supporting Information).

Finally, we verified the feasibility of employing the LIG-based bioelectrodes as a neural interface for recording and stimulating applications in a rat model, as schematically illustrated in Figure 5a. During the stimulation session, the primary motor cortex (M1) was targeted to induce hind limb movement, while in the recording experiment, cortical potentials were monitored from the whisker somatosensory barrel cortex (wS1) in response to tactile stimulation of the whisker. Throughout the experiments, the electrodes were positioned and secured using a micromanipulator, while the head of the animal was firmly immobilized using a stereotaxic frame. Precise electrical stimulation of M1, which is associated with executing voluntary movements, can elicit movements in the heel, such as dorsiflexion (i.e., lifting the heel) or plantarflexion (i.e., pointing the toes and lowering the heel). This allows for a deeper exploration of the neural mechanisms involved in movement control and holds potential in clinical applications for assisting patients with motor impairments. Further, since the wS1 region is responsible for receiving and processing sensory information from the body, including touch, pain, and proprioception, monitoring cortical activity from the wS1 upon a tactile sensation of whiskers can identify the neural connectivity within the sensory network. First, as demonstrated in Figure 5b, a stereotaxic technique was employed to position the LIG-based microelectrode array onto the right M1 region. Subsequently, a series of symmetric biphasic current pulses with a 3 mA amplitude was applied, with increasing pulse durations from 100 to 500 μs . During the stimulation, the animals were video-recorded to track the trajectories of the toe and heel of the left hind limb, which were quantitatively analyzed using a deep learning-based markerless feature-tracking algorithm,^[74–76] as presented in Supporting Movie S4, Supporting Information (see the details in Section 4). As displayed in Figure 5b (right graph), the extracted coordinates of the toe and heel in response to varying stimulation strengths were normalized with respect to

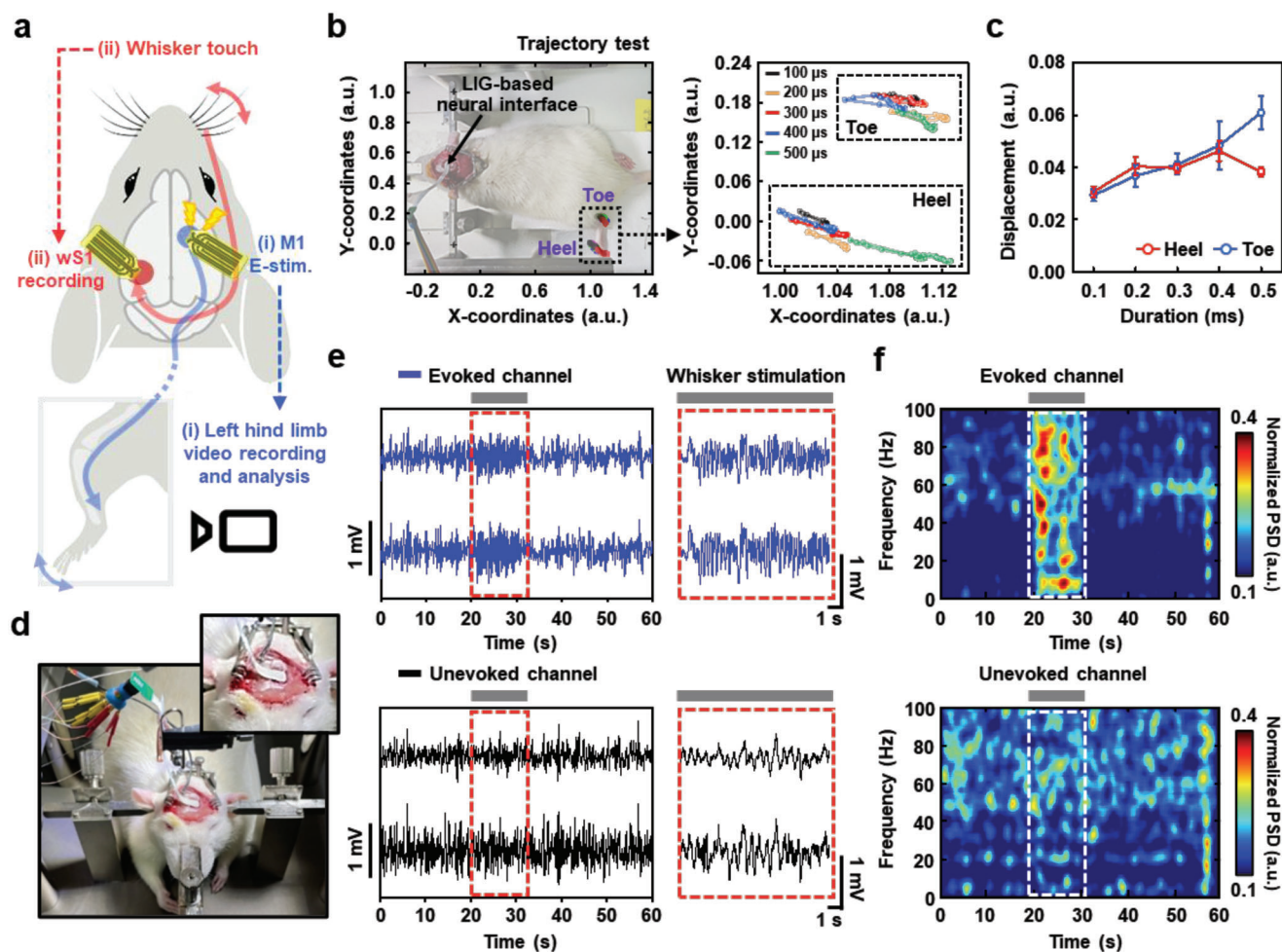


Figure 5. a) Schematic illustration of in vivo experiments using a rat model: i) cortical stimulation of M1 region to induce hind limb movement, and ii) cortical recording from wS1 region in response to whisker touching. b,c) M1 stimulation with markerless video-tracking of toe and heel trajectories in response to increasing pulse durations duration ($n = 5$ for each experiment at different durations), representing a linear relationship of peak displacement and pulse duration. d) Digital images of the stereotaxic technique for signal acquisition from the barrel cortex with the LIG-based microelectrode array. e) Representative LFP signals from the evoked and unevoked channels upon whisker-touching stimulation (stimulation period is marked by red dotted boxes). f) Spectrograms of the recorded LFP signals indicate the increased power responses during the stimulated period of 20–30 s (marked by white dotted boxes). The power spectral densities for each frequency were normalized between 0 and 1.

two reference endpoints of the stereotaxic frame in order to compensate for variations in the positions across the experimental sessions. The combined displacement of toes and heels relative to the rest positions, as temporally aligned by the onset of stimulation in Figure S25, Supporting Information, demonstrates an increasing magnitude of movements induced by stronger stimulation (i.e., longer pulse duration). As shown in Figure 5c, the maximum displacements exhibited a linear relationship with increasing strengths of stimulation, thus confirming the effective modulation of motor function using the LIG-based bioelectrodes. Next, the evoked cortical responses were recorded from the surface of the left barrel cortex using the subdurally implanted LIG-based microelectrode array in an anesthetized adult rat (Figure 5a,ii). As depicted in Figure 5d, the position of recording sites was adjusted along the coordinates to conformally place the LIG electrodes on the target region. Figure 5e presents representative segments of local field potential (LFP) recordings for 60

s, during which the touching stimulation was applied to the right whiskers for 10 s (marked by red dotted boxes; see Figure S26, Supporting Information, for the signals from 8 channels). These recorded signals exhibited typical slow up-down dynamics with oscillations associated with a sleep-like state of rats induced by urethane anesthesia. Notably, the magnified waveforms between 20 to 30 s in the right panel of Figure 5e revealed distinct touch-induced activities with high-frequency oscillations from the channels at the corresponding whisker area. To further analyze the collected signals in the time-frequency domain, spectrograms were computed in the 0–100 Hz frequency band during the same stimulation period, as shown in Figure 5f. The upper graph of the representative spectrogram from one of the evoked channels clearly demonstrated a significant increase in power spectral density (PSD) during the stimulation, compared to the resting states. In contrast, the lower spectrogram from channels outside the evoked area (i.e., unevoked channels) did not exhibit noticeable

spectral responses during the whisker stimulation session. The successful LFP recording with a tactile input and the modulation of motor functions through cortical stimulation suggest the feasibility of the proposed LIG-based bioelectrode on LCP and its potential utilization in various neural interface applications.

3. Conclusion

In summary, we have developed flexible and stretchable electrode arrays by leveraging the robust characteristics of the carbon nanomaterial through focused laser irradiation on the new source material (i.e., LCP film). By utilizing the LCP film as a biocompatible electronic substrate, we have demonstrated precise control over laser exposure parameters, pattern generation, and transfer printing processes, enabling the manufacturing of patterned LIG-based bioelectrodes. Especially, the resolution of the patterned LIG film array has significantly improved through the implementation of a shadow masking process during laser scanning on the LCP film surface. Our high-throughput strategy for the circuit writing and SMD integration with supporting materials in a flexible format maximizes the value of the LIG/LCP material by fully utilizing the advantageous material's features such as high flexibility and low moisture absorption, thereby enabling its application on tissue surfaces such as human skin and animal brain. In particular, our kirigami-inspired on-skin bioelectrodes exhibit a reasonable stretchability ($\approx 30\%$) and can be independently connected to healthcare hardware platforms for ECG and EMG measurements. Furthermore, by combining with mechanically compliant architectures, we suggest a brain-interfaced LIG microelectrode that integrates the current source for stimulation and recording while encapsulating the same LCP material, with superior electrochemical performance. We believe that our newly developed approach for producing a patterned array of the LIG bioelectrode offers a cost-effective, scalable, and simple encapsulation route to achieve biocompatible bioelectrodes composed of laser-converted graphene. Such bioelectrodes serve as ideal circuit-enabled flexible substrates for other promising applications, ensuring long-term reliability in the body's ionic environment.

4. Experimental Section

The Fabrication of LIG: LCP film (Vecstar CTQ-25, Kuraray) was used to produce the LIG electrode as received. Direct writing of the patterned LIG films was performed using a customized laser system (450 nm, Ideal Korea, South Korea) with 0.8–1.5 mm of beam diameter (the focused laser spot size was measured to be $\approx 250 \mu\text{m}$) with a maximum power of 3 W and a scanning speed of $\approx 1 \text{ mm s}^{-1}$ and the step interval of $\approx 50 \mu\text{m}$. To enhance the resolution of the patterned LIG films, laser beam parameters were optimized at the power of 1.5–2.25 W. All of the laser experiments were performed under ambient conditions.

LIG-Based Kirigami Electrodes: After the formation of LIG on an LCP film (2.25 mW, 5 scans), the LIG/LCP substrate was conformally attached to an adhesive PET film (100 μm) to secure the durability of the LIG film, and the contact area with skin was covered with a conductive hydrogel. Next, the PET/LIG/hydrogel substrate was mechanically cut into the designed structure by using a computer-controlled dicing machine. The connected triangular blocks (6 \times 6 units) in the layered patch-type electrode (i.e., PET/LCP/LIG/hydrogel film) were produced with closed and open configurations.

LIG-Based Biosensor and Electrochemical Measurements: To fabricate the LIG-based TNF- α biosensor, the 3-terminal LIG electrodes were generated as working ($D = 8 \text{ mm}$), counter, and reference electrodes (laser power of $\approx 2.1 \text{ W}$, 5 scans), and speeds ($\approx 1 \text{ mm s}^{-1}$). The patterned LIG/LCP substrate was then transferred to a PET substrate (i.e., handling substrate). Subsequently, WE was modified with 5 mm 1-pyrenebutyric acid (1-PBA) in DMSO for 60 min and was immersed in an EDC/NHS aqueous solution (each 50 mM) for 90 min, followed by an anti-TNF α antibodies solution (10 $\mu\text{g mL}^{-1}$, in 0.01 M PBS buffer) was loaded; the prepared biosensors were rinsed with DI water to remove physically bonded antibodies. Finally, the free carboxyl end groups were blocked by the BSA (10 $\mu\text{g mL}^{-1}$, in 0.01 M PBS buffer), forming a chemically modified biosensor electrode (i.e., LIG/1-PBA/NHS-EDC/Ab-TNF- α /BSA). The properties of the prepared impedimetric biosensor were monitored in a 1 mL aqueous PBS solution (0.01 M, pH = 7.4) containing a redox probe (10 mM ferri/ferrocyanide, $[\text{Fe}(\text{CN})_6]^{3-/4-}$) during the electron transfer process. By applying TNF- α in 0.01 M PBS solution, the value changes of impedance were measured at each specific standard concentration, ranging from 10 to 200 pg mL^{-1} for 60 min. The EIS was recorded at 10 mV amplitude and 0.05–100 kHz frequency with 0.1 V potential.

Materials Characterization: To confirm the laser-induced carbonization of LCP film, thermogravimetric analysis (TGA 55, TA Instruments, USA) was carried out between 25–700 $^\circ\text{C}$ at 10 $^\circ\text{C min}^{-1}$ under air and N_2 conditions. The surface morphology of LIG was investigated using optical microscopy (OM, BX 51, Olympus, Japan) and SEM (Carl Zeiss AG-SUPRA 40 VP, Germany). The quality of LIG films, according to the laser power and the numbers of operated scans, was evaluated by Raman spectroscopy with 532 nm laser excitation (NS220, Nanoscope Systems, South Korea). The sheet resistances of LIG electrodes by changing the laser power/scans were measured using a parameter analyzer (Agilent 4156A, Agilent Technologies, Santa Clara, USA) in ambient conditions. EDX mapping was also conducted as a quantitative elemental analysis to ensure the composition and byproduct during the processes, such as C, O, Na, K, and Cl, on the LCP film, LIG, laminated LIG, and CV-activated LIG electrode. The surface chemical states of LCP film, LIG, laminated LIG, and CV-activated LIG electrode were determined by XPS (Kratos Analytical, AXIS SUPRA, Japan) with an Al-K α excitation source (1486.6 eV). All the spectra were corrected using C1s peaks (284.8 eV) as references. The tensile strength of the LIG-structured films was measured by a texture analyzer (CT3, Brookfield Engineering, USA). LIG-structured film was fabricated in size to 10 \times 10 mm^2 on LCP film (100 \times 10 mm^2). Next, the specimen was firmly fixed to both ends of the LCP film at intervals of 20 mm. Next, the specimen was firmly fixed to both ends of the LCP film at intervals of 20 mm. The tensile strength and elongation of the LIG-structured film were measured while pulling the upper clamp at a test speed of 0.1 mm s^{-1} .

Cytotoxicity Evaluation of LIG Electrode: The cytotoxicity of the LIG electrode was confirmed by cell counting kit-8 (CCK-8, Dojindo Molecular Technologies Inc., Kumamoto, Japan) and lactate dehydrogenase (LDH) assays (Takara Bio Inc., Shiga, Japan). To prepare the substrates, the fully covered LIG on LCP film was transferred to a flat PDMS film with a size of 1.5 \times 1.5 cm^2 , on which a laminin solution (50 $\mu\text{g mL}^{-1}$) was subsequently dropped on LIG/PDMS substrate and incubated at 37 $^\circ\text{C}$ for 2 h. Next, L-929 murine fibroblast cells were cultured in a DMEM medium containing 10% fetal bovine serum (FBS) and 1% penicillin–streptomycin at 37 $^\circ\text{C}$ with 5% CO_2 in an incubator. The cells were seeded in the laminin-coated LIG/PDMS substrate at a density of 5 \times 10³ cells mL^{-1} and were incubated for 24 and 48 h. For the cytotoxicity evaluation, CCK-8 solution was added to each well plate for 2 h of the culture at 37 $^\circ\text{C}$ in the dark, and the absorbance was measured at 450 nm using a microplate reader. For an additional LDH assay, LDH solution was added to each well plate and then incubated for 30 min at room temperature in the dark, and the absorbance was measured at 490 nm using a microplate reader (SpectraMax 340, Molecular Device Co., Sunnyvale, USA).

Encapsulation for LCP-LIG-LCP Electrode Array: The LIG electrode array on the LCP film was encapsulated by a 25- μm -thick, lower-melting-point LCP cover layer (Vecstar CTF-25, Kuraray) via a laminating process as described in previous publications.^[30,77] Briefly, the cover layer was prepared by a UV laser cutting machine (Samurai Desktop 3500, DPSS Laser, USA)

to define opening windows. The LCP substrate attached with the cover layer on a 4-in. silicon wafer was mounted within a pair of metal jigs for alignment, and thermally pressed (285 °C, 30 kg load for 15 min) using a heating press (model 3851, Carver, USA). The LCP-LIG array was completed after outlining using UV laser. The LCP-LIG microelectrode array was directly connected to a commercially available 0.5 mm-pitch 8-channel flexible flat cable (FFC) using anisotropic conductive film (ACF; AC2056R-35, Showa Denko, Japan). The ACF was first attached to the pads area of the array by pressing with a pair of slide glasses and foldback clips, followed by baking for 10 min in a drying oven at 70 °C. After removing the liner layer, FFC was aligned and bonded to ACF film at 160 °C for 10 min to form electrical conduction. A custom-designed PCB interface board was used for addressing each channel to the stimulator and recording instruments.

Electrochemical Activation and Evaluation: The proposed electrochemical activation process for enhancing the electrochemical properties of LIG electrodes consists of repeated voltage scanning in the range of -2 V to 1.5 V (vs Ag/AgCl) at 50 mV s^{-1} in PBS. The electrochemical performance of the LIG microelectrode array before and after the activation process was evaluated by EIS, CV, and voltage transient measurements in PBS. The EIS and CV were measured by a potentiostat (CompactStat, Ivium Technologies, Netherlands) in a three-electrode configuration with Ag/AgCl and Pt electrodes as reference and counter electrodes, respectively. The EIS data in the frequency range from 1 Hz to 1 MHz were curve-fitted to the equivalent circuit model using ZView (Scribner Associates, USA),^[65,66] and they were quantitatively compared to the electrochemical behaviors of the LIG electrode before/after the activation processes ($n = 17$ each for before and after the activation). A comparison of the measured EIS values and the fitted curves using the equivalent circuit model is presented in Figure S19, Supporting Information, demonstrating reliable fitting results in the entire frequency ranges. The CV curves were measured at a scan rate of 50 mV s^{-1} in the voltage range from -1.5 V to 1 V (vs Ag/AgCl electrode), which was determined as the maximum potential window of the LIG electrodes without inducing oxidation nor reduction. The CSC_C values were calculated by integrating the cathodic current of the CVs. Voltage transients were monitored to evaluate the maximum charges that can be injected in a single stimulation pulse without exceeding the water window limit of LIG electrodes. Biphasic, cathodic-first, and charge-balanced current pulses were applied to the fabricated microelectrodes in PBS solution using a stimulus generator (STG4008, Multi-Channel Systems MCS GmbH, Germany). The WE and counter electrode were used to deliver the current pulses of varying amplitudes at a fixed pulse duration of 400 ms per phase and an inter-phase period of 60 ms, while the voltage excursion between WE and the reference electrode was measured using an oscilloscope (DPO 4034, Tektronix, USA). The CIC of the LIG electrode was calculated from the critical current amplitude above which the maximum positive (E_{ma}) or negative polarization potential (E_{mc}) exceeds the water window of the LIG electrodes.

Animals and Surgery Procedures: All procedures were conducted in accordance with National Institutes of Health guidelines and approved by the Institution Animal Care and Use Committee (IACUC) of Yonsei University (2019-0228). Male Sprague-Dawley rats weighing 300 – 350 g were used in this study. The light was controlled under a 12 h light/dark (light on between 07:00 a.m. and 07:00 p.m.) cycle. The temperature was maintained at 22 ± 2 °C and relative humidity was at $55 \pm 5\%$. Animals were allowed to acclimate for at least a week before surgery. Rats were anesthetized using urethane (1.25 g/kg/i.p.) and placed in a stereotaxic frame. The rats' heads were disinfected by povidone-iodine, and the midline incisions were made.

In Vivo Neural Stimulation and Data Analysis: For in vivo stimulation test, a 5×5 mm craniotomy was performed to expose the right primary motor cortex for inducing movement in the left hind limb. The bonny window exposed 1 mm anteriorly and 4 mm posteriorly based on bregma and 1 – 6 mm laterally to the midline. Cathodic-first symmetric biphasic current pulses with 3 mA amplitude with varying pulse duration from 100 to 500 ms were applied through the electrode arrays. A stimulus consists of a burst of 200 biphasic pulses, which were repeated 5 times with 3 s intervals for a single stimulation session. The movements of the left hind

limb, in response to the cortical stimulation, were recorded using a camera fixated above the animals (30 frames s^{-1} , 1920×1080 pixels). The recorded video files were analyzed by a deep learning algorithm to extract the positions of toes and heels in each frame, for quantitative analysis of behavioral responses of animals upon cortical stimulation with varying strengths. The feature extraction was conducted using DeepLabCut, an open-source toolbox for markerless pose estimation of animals performing various tasks.^[74–76] Four distinct points (toe, heel, and two reference points from the stereotaxic frame) were labeled from a dataset of ≈ 20 frames after excluding ≈ 10 unnecessary frames selected from k -means clustering.

In Vivo Neural Recording: For the recording session, a 5×5 mm craniotomy was performed to expose the right barrel cortex for capturing cortical responses to the physical stimulation of left whiskers. The cranial window was exposed from 0 to 5 mm posterior to the bregma and 2 – 7 mm lateral to the midline. Dura was carefully removed using a 31 G needle and micro forceps. A burr hole was made in the left parietal bone and a screw was placed to work as a reference electrode. An LCP-LIG-LCP microelectrode array was placed over the exposed barrel cortical area using a micro-manipulator. Simultaneous neural recordings from the 8 electrodes were performed with CED1401 (Cambridge Electronic Design Limited, U.K.) at a sampling frequency of 25 kHz. To induce cortically evoked responses, touching stimulation was applied on the right whisker for 10 s (from $t = 20$ – 30 s during total 60 s recording session). The analysis of neural signals was executed by MATLAB program with customized codes. The power spectral densities derived from the measured signals were normalized to a range of 0 – 1 for each frequency.

Statistical Analysis: All the data with error bars represent the mean \pm standard deviation. The sample or repetition numbers for each dataset were indicated in the figure captions. For the analysis of equivalent circuit parameters (in Figure S19, Supporting Information), box plots were used to display data from the 25th to the 75th percentile, with the median represented by the central line. Statistical significance among two different sample groups (i.e., non-activation and activation groups) was analyzed by Wilcoxon signed-rank test using MATLAB. Statistical significance is indicated as follows: n.s. (not significant), * (for $p < 0.05$), ** (for $p < 0.01$), *** (for $p < 0.001$).

Supporting Information

Supporting Information is available from the Wiley Online Library or from the author.

Acknowledgements

R.P., D.H.L., and C.S.K. contributed equally to this work. This work was supported by the Korea Medical Device Development Fund grant funded by the Korean Government (the Ministry of Science and ICT, the Ministry of Trade, Industry and Energy, the Ministry of Health and Welfare, the Ministry of Food and Drug Safety) (NTIS Number: 9991006781, KMDF_PR_20200901_0108). This work was supported by the National Research Foundation of Korea (NRF) grant funded by the Ministry of Science and ICT, Republic of Korea (2021R1A5A1032937, 2022R1C1C1010422, 2023R1A2C2006405). The experiments in Figures 2d and 3 were not subject to ethical approval in the authors' institute, although participants did take part following written informed consent.

Conflict of Interest

The authors declare no conflict of interest.

Data Availability Statement

The data that support the findings of this study are available from the corresponding author upon reasonable request.

Keywords

bioelectrodes, graphene, lasers, liquid crystal polymers, neural interfaces

Received: June 2, 2023

Revised: October 9, 2023

Published online: November 12, 2023

- [1] J. Lin, Z. Peng, Y. Liu, F. Ruiz-Zepeda, R. Ye, E. L. G. Samuel, M. J. Yacamán, B. I. Yakobson, J. M. Tour, *Nat. Commun.* **2014**, *5*, 5714.
- [2] Y. Yang, Y. Song, X. Bo, J. Min, O. S. Pak, L. Zhu, M. Wang, J. Tu, A. Kogan, H. Zhang, T. K. Hsiai, Z. Li, W. Gao, *Nat. Biotechnol.* **2020**, *38*, 2175.
- [3] S. Rauf, A. A. Lahcen, A. Aljedaibi, T. Beduk, J. Ilton De Oliveira Filho, K. N. Salama, *Biosens. Bioelectron.* **2021**, *180*, 113116.
- [4] R. Ye, D. K. James, J. M. Tour, *Acc. Chem. Res.* **2018**, *51*, 1609.
- [5] Y. Li, J. Long, Y. Chen, Y. Huang, N. Zhao, *Adv. Mater.* **2022**, *34*, 2200517.
- [6] H. Wang, Z. Zhao, P. Liu, X. Guo, *Biosensors* **2022**, *12*, 55.
- [7] R. Park, H. Kim, S. Lone, S. Jeon, Y. Kwon, B. Shin, S. Hong, *Sensors* **2018**, *18*, 1857.
- [8] F. M. Vivaldi, A. Dallinger, A. Bonini, N. Poma, L. Sembranti, D. Biagini, P. Salvo, F. Greco, F. Di Francesco, *ACS Appl. Mater. Interfaces* **2021**, *13*, 30245.
- [9] A. A. Lahcen, S. Rauf, T. Beduk, C. Durmus, A. Aljedaibi, S. Timur, H. N. Alshareef, A. Amine, O. S. Wolfbeis, K. N. Salama, *Biosens. Bioelectron.* **2020**, *168*, 112565.
- [10] M. G. Stanford, J. T. Li, Y. Chyan, Z. Wang, W. Wang, J. M. Tour, *ACS Nano* **2019**, *13*, 7166.
- [11] H. Wang, H. Wang, Y. Wang, X. Su, C. Wang, M. Zhang, M. Jian, K. Xia, X. Liang, H. Lu, S. Li, Y. Zhang, *ACS Nano* **2020**, *14*, 3219.
- [12] H. Park, M. Kim, B. G. Kim, Y. H. Kim, *ACS Appl. Nano Mater.* **2020**, *3*, 6899.
- [13] Y. Lee, M. J. Low, D. Yang, H. K. Nam, T.-S. Dinh Le, S. E. Lee, H. Han, *Light: Sci. Appl.* **2023**, *12*, 146.
- [14] T.-S. D. Le, H.-P. Phan, S. Kwon, S. Park, Y. Jung, J. Min, B. J. Chun, H. Yoon, S. H. Ko, S.-W. Kim, Y.-J. Kim, *Adv. Funct. Mater.* **2022**, *32*, 2205158.
- [15] S. M. Won, E. Song, J. Zhao, J. Li, J. Rivnay, J. A. Rogers, *Adv. Mater.* **2018**, *30*, 1800534.
- [16] H. Lee, C. Song, Y. S. Hong, M. S. Kim, H. R. Cho, T. Kang, K. Shin, S. H. Choi, T. Hyeon, D.-H. Kim, *Sci. Adv.* **2017**, *3*, e1601314.
- [17] C. Fenzl, P. Nayak, T. Hirsch, O. S. Wolfbeis, H. N. Alshareef, A. J. Baeumner, *ACS Sens.* **2017**, *2*, 616.
- [18] M. d'Amora, A. Lamberti, M. Fontana, S. Giordani, *J. Phys. Mater.* **2020**, *3*, 034008.
- [19] W. Wang, B. Han, Y. Zhang, Q. Li, Y.-L. Zhang, D.-D. Han, H.-B. Sun, *Adv. Funct. Mater.* **2021**, *31*, 2006179.
- [20] J. Li, Y. Liu, L. Yuan, B. Zhang, E. S. Bishop, K. Wang, J. Tang, Y.-Q. Zheng, W. Xu, S. Niu, L. Beker, T. L. Li, G. Chen, M. Diyaolu, A.-L. Thomas, V. Mottini, J. B. H. Tok, J. C. Y. Dunn, B. Cui, S. P. Paşca, Y. Cui, A. Habtezion, X. Chen, Z. Bao, *Nature* **2022**, *606*, 94.
- [21] S. M. Won, L. Cai, P. G. Putruf, J. A. Rogers, *Nat. Biomed. Eng.* **2021**, *7*, 405.
- [22] Y. Lu, H. Lyu, A. G. Richardson, T. H. Lucas, D. Kuzum, *Sci. Rep.* **2016**, *6*, 33526.
- [23] C. Hassler, T. Boretius, T. Stieglitz, *J. Polym. Sci., Part B: Polym. Phys.* **2011**, *49*, 18.
- [24] A. Buyle Padias, H. K. Hall Jr., *Polymers* **2011**, *3*, 833.
- [25] Y. Ji, Y. Bai, X. Liu, K. Jia, *Adv. Ind. Eng. Polym. Res.* **2020**, *3*, 160.
- [26] A.-V. Pham, *IEEE Microwave Mag.* **2011**, *12*, 83.
- [27] L. C. Sawyer, A. Kaslusky, in *Encyclopedia of Materials: Science and Technology*, Elsevier, Amsterdam **2001**, p. 5155.
- [28] A. D. Mohanty, C. Bae, *Adv. Organomet. Chem.* **2015**, *64*, 1.
- [29] J. Jeong, K. S. Min, S. J. Kim, *Microelectron. Eng.* **2019**, *216*, 111096.
- [30] S. W. Lee, K. S. Min, J. Jeong, J. Kim, S. J. Kim, *IEEE Trans. Biomed. Eng.* **2011**, *58*, 2255.
- [31] A. F. Carvalho, A. J. S. Fernandes, C. Leitão, J. Deuermeier, A. C. Marques, R. Martins, E. Fortunato, F. M. Costa, *Adv. Funct. Mater.* **2018**, *28*, 1805271.
- [32] Q. Li, T. Wu, W. Zhao, Y. Li, J. Ji, G. Wang, *Composites, Part B* **2022**, *240*, 110000.
- [33] R. Ye, Y. Chyan, J. Zhang, Y. Li, X. Han, C. Kittrell, J. M. Tour, *Adv. Mater.* **2017**, *29*, 1702211.
- [34] S. Lee, S. Jeon, *ACS Sustainable Chem. Eng.* **2019**, *7*, 2270.
- [35] L. X. Duy, Z. Peng, Y. Li, J. Zhang, Y. Ji, J. M. Tour, *Carbon* **2018**, *126*, 472.
- [36] Z. Wang, K. K. Tan, Y. C. Lam, *Micromachines* **2021**, *12*, 227.
- [37] Y. Chen, J. Long, S. Zhou, D. Shi, Y. Huang, X. Chen, J. Gao, N. Zhao, C.-P. Wong, *Small Methods* **2019**, *3*, 1900208.
- [38] A. C. Ferrari, J. C. Meyer, V. Scardaci, C. Casiraghi, M. Lazzeri, F. Mauri, S. Piscanec, D. Jiang, K. S. Novoselov, S. Roth, A. K. Geim, *Phys. Rev. Lett.* **2006**, *97*, 187401.
- [39] D. Yi, S. Jeon, S. W. Hong, *ACS Appl. Mater. Interfaces* **2018**, *10*, 40014.
- [40] B. Sun, R. N. McCay, S. Goswami, Y. Xu, C. Zhang, Y. Ling, J. Lin, Z. Yan, *Adv. Mater.* **2018**, *30*, 1804327.
- [41] S. Heo, J. Ha, S. J. Son, I. S. Choi, H. Lee, S. Oh, J. Jekal, M. H. Kang, G. J. Lee, H. H. Jung, J. Yea, T. Lee, Y. Lee, J.-W. Choi, S. Xu, J. H. Choi, J.-W. Jeong, Y. M. Song, J.-C. Rah, H. Keum, K.-I. Jang, *Sci. Adv.* **2021**, *7*, eabh0040.
- [42] A. Carlson, A. M. Bowen, Y. Huang, R. G. Nuzzo, J. A. Rogers, *Adv. Mater.* **2012**, *24*, 5284.
- [43] S. Jeon, R. Park, J. Jeong, G. Heo, J. Lee, M. C. Shin, Y. W. Kwon, J. C. Yang, W. I. Park, K. S. Kim, J. Park, S. W. Hong, *Small* **2021**, *17*, 2105733.
- [44] S. Liu, Y. Rao, H. Jang, P. Tan, N. Lu, *Matter* **2022**, *5*, 1104.
- [45] R.-H. Kim, M.-H. Bae, D. G. Kim, H. Cheng, B. H. Kim, D.-H. Kim, M. Li, J. Wu, F. Du, H.-S. Kim, S. Kim, D. Estrada, S. W. Hong, Y. Huang, E. Pop, J. A. Rogers, *Nano Lett.* **2011**, *11*, 3881.
- [46] M. Sharifuzzaman, M. A. Zahed, M. S. Reza, M. Asaduzzaman, S. Jeong, H. Song, D. K. Kim, S. Zhang, J. Y. Park, *Adv. Funct. Mater.* **2023**, *33*, 2208894.
- [47] Y. Ling, W. Pang, X. Li, S. Goswami, Z. Xu, D. Stroman, Y. Liu, Q. Fei, Y. Xu, G. Zhao, B. Sun, J. Xie, G. Huang, Y. Zhang, Z. Yan, *Adv. Mater.* **2020**, *32*, 1908475.
- [48] K. Xu, Y. Fujita, Y. Lu, S. Honda, M. Shiomi, T. Arie, S. Akita, K. Takei, *Adv. Mater.* **2021**, *33*, 2008701.
- [49] X. Ning, X. Wang, Y. Zhang, X. Yu, D. Choi, N. Zheng, D. S. Kim, Y. Huang, Y. Zhang, J. A. Rogers, *Adv. Mater. Interfaces* **2018**, *5*, 1800284.
- [50] X. Shang, L. Liu, A. Rafsanjani, D. Pasini, *J. Mater. Res.* **2018**, *33*, 300.
- [51] A. Rafsanjani, D. Pasini, *Extreme Mech. Lett.* **2016**, *9*, 291.
- [52] Q. Guan, B. Norder, T. J. Dingemans, *J. Appl. Polym. Sci.* **2017**, *134*, 44774.
- [53] X. Qu, Y. W. Kwon, S. Jeon, J. Jeong, W. Kang, Z. Jiang, C. Zhang, S. W. Hong, *J. Colloid Interface Sci.* **2023**, *634*, 715.
- [54] P. C. A. Kam, N. I. Ferch, *Anaesthesia* **2000**, *55*, 1081.
- [55] J. Martínez-Borra, C. López-Larrea, S. González, D. Fuentes, A. Dieguez, E. M. Deschamps, J. M. Pérez-Pariente, A. López-Vázquez, R. D. Francisco, L. Rodrigo, *Am. J. Gastroenterol.* **2002**, *97*, 2350.
- [56] J. Liu, Y. Duan, *Oral Oncol.* **2012**, *48*, 569.
- [57] M. Wang, Y. Yang, W. Gao, *Trends Chem.* **2021**, *3*, 969.
- [58] W. Yang, Y. Gong, W. Li, *Front. Bioeng. Biotechnol.* **2021**, *8*, 622923.

- [59] J. Jeong, S. Hyun Bae, J.-M. Seo, H. Chung, S. June Kim, *J. Neural Eng.* **2016**, *13*, 025004.
- [60] Y. Cho, S. Park, J. Lee, K. J. Yu, *Adv. Mater.* **2021**, *33*, 2005786.
- [61] S. M. Yang, J. H. Shim, H.-U. Cho, T.-M. Jang, G.-J. Ko, J. Shim, T. H. Kim, J. Zhu, S. Park, Y. S. Kim, S.-Y. Joung, J. C. Choe, J.-W. Shin, J. H. Lee, Y. M. Kang, H. Cheng, Y. Jung, C.-H. Lee, D. P. Jang, S.-W. Hwang, *Adv. Mater.* **2022**, *34*, 2108203.
- [62] A. Cissal, F. R. Ihmig, J. C. Fraile, J. P. Turiel, V. Muñoz-Martinez, *Sensors* **2019**, *19*, 2725.
- [63] D.-J. Hsu, Y.-W. Chi, K.-P. Huang, C.-C. Hu, *Electrochim. Acta* **2019**, *300*, 324.
- [64] Q. Cheng, J. Tang, J. Ma, H. Zhang, N. Shinya, L.-C. Qin, *Carbon* **2011**, *49*, 2917.
- [65] W. Wang, S. Guo, I. Lee, K. Ahmed, J. Zhong, Z. Favors, F. Zaera, M. Ozkan, C. S. Ozkan, *Sci. Rep.* **2014**, *4*, 9.
- [66] T. Gu, B. Wei, *Nanoscale* **2015**, *7*, 11626.
- [67] J. Zhao, X. Zou, Y. Zhu, Y. Xu, C. Wang, *Adv. Funct. Mater.* **2016**, *26*, 8103.
- [68] Q. Cheng, J. Tang, J. Ma, H. Zhang, N. Shinya, L.-C. Qin, *Phys. Chem. Chem. Phys.* **2011**, *13*, 17615.
- [69] C. Choi, D. S. Ashby, D. M. Butts, R. H. DeBlock, Q. Wei, J. Lau, B. Dunn, *Nat. Rev. Mater.* **2020**, *5*, 5.
- [70] Y. Liu, S. P. Jiang, Z. Shao, *Mater. Today Adv.* **2020**, *7*, 100072.
- [71] N. V. Apollo, M. I. Maturana, W. Tong, D. A. X. Nayagam, M. N. Shivdasani, J. Foroughi, G. G. Wallace, S. Praver, M. R. Ibbotson, D. J. Garrett, *Adv. Funct. Mater.* **2015**, *25*, 3551.
- [72] K. Wang, C. L. Frewin, D. Esrafilzadeh, C. Yu, C. Wang, J. J. Pancrazio, M. Romero-Ortega, R. Jalili, G. Wallace, *Adv. Mater.* **2019**, *31*, 1805867.
- [73] D. W. L. Hukins, A. Mahomed, S. N. Kukureka, *Med. Eng. Phys.* **2008**, *30*, 1270.
- [74] S. Williams, Z. Zhao, A. Hafeez, D. C. Wong, S. D. Relton, H. Fang, J. E. Alty, *J. Neurol. Sci.* **2020**, *416*, 117003.
- [75] T. Nath, A. Mathis, A. C. Chen, A. Patel, M. Bethge, M. W. Mathis, *Nat. Protoc.* **2019**, *14*, 2152.
- [76] A. Mathis, P. Mamidanna, K. M. Cury, T. Abe, V. N. Murthy, M. W. Mathis, M. Bethge, *Nat. Neurosci.* **2018**, *21*, 1281.
- [77] J. Jeong, S. Hyun Bae, K. S. Min, J.-M. Seo, H. Chung, S. June Kim, *IEEE Trans. Biomed. Eng.* **2015**, *62*, 982.